Utrecht University Nikhef

Master Thesis
June 22, 2018

First observation of the decay $\Lambda_b^0 \to D_s^- p$

Author: M. J. Tervoert, BSc
PhD Supervisor: L. J. Bel, MSc
Supervisors: dr. N. Tuning
dr. A. Mischke
dr. A. G. Grelli

Abstract

In this thesis, we present the first observation of the decay $\Lambda_b^0 \to D_s^- p$ with a significance of 20σ using proton-proton data collected with the LHCb at $\sqrt{s} = 7\,\text{TeV}$, $\sqrt{s} = 8\,\text{TeV}$, and $\sqrt{s} = 13\,\text{TeV}$, corresponding to a total integrated luminosity of $4.9\,\text{fb}^{-1}$. Furthermore, considering the normalisation decay $\Lambda_b^0 \to \Lambda_c^+ \pi^-$, we report a branching fraction of $B(\Lambda_b^0 \to D_s^- p) = (10.7 \pm 1.2) \times 10^{-6}$ (excluding systematic uncertainties). This result could help understanding the long standing discrepancy on the value of $|V_{ub}|$.

Acknowledgements

First and foremost, I would like to thank my supervisors, Niels Tuning and Lennaert Bel. Niels, even though you were at CERN most of the time as an extremely busy Run Coordinator, you were still able to make time for weekly meetings and were always able to make time for questions. I am very grateful for your unlimited positivity and enthusiasm and I greatly enjoyed all discussions about various aspects of the analysis. Lennaert, thank you for all the time you were able to help in countless different ways. I am very grateful for all discussions we had, whether it was about physics or when I needed help with another coding problem in python or LaTeX. I would like to thank you both and Sevda Esen, for reading my thesis several times, your comments greatly improved the quality of this final version.
Besides my daily supervisors Niels and Lennaert, I would also like to thank my supervisors from Utrecht University André Mischke and Alessandro Grelli, for comments on my draft version, and reading the final version.
I would like to specially thank Michele Veronesi, Sevda Esen, and also Lennaert Bel, for all the constructive input. Sevda, an incredible thank you for all the simulation data you were able to generate for me. Michele and Lennaert, thank you for all the ntuples you made (and remade) for me.
I am very grateful for Agnieszka Dziurda for making the fit of the $\Lambda_b^0 \to D_s^- p$ decay, the analysis would not have been possible without your help with the B2DXFitter package. Your work and input is greatly appreciated.
Furthermore, I would like to give a thanks to the entire b-physics group at Nikhef, for all input everyone gave. I would especially like to thank everyone I shared the master room with, you all made the work a lot more fun throughout the entire year.
Last, but definitely not least, I would like to thank my family and friends, who gave me the continuous support throughout the year. I would like to thank everyone who read my thesis, and gave constructive feedback on the physics aspect and picked out many spelling errors, typos, and odd sentence structures. I am extremely grateful for all support you gave me these last ten months.

Contents

Chapter 1

Introduction

The Standard Model is exceptionally successful in describing all particles we currently know of, and the interactions between them. The Standard Model is visualised in Fig. 1.1, where we see the three generations of quarks and leptons. Experimental results from Z boson decays and Higgs production suggest that there are precisely three generations of leptons, however, this measurement is not able to make the same prediction for quarks. The question arises if there might be a fourth generation of quarks, and if not, why there are exactly three generations of quarks as well.

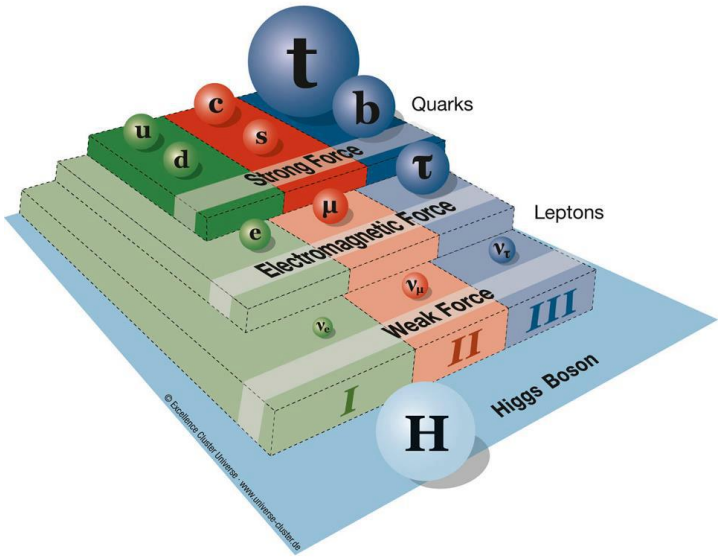

Figure 1.1 – A visualisation of the Standard Model. The sizes of the spheres represent the relative masses of the fundamental particles where the three colours represent the three generations of particles. The particles are affected by the force block they are standing on plus the ones underneath. The force carriers, the gluons (g) for the strong force, photons (γ) for the electromagnetic force and the Gauge bosons ($W^{\pm}$ and Z) for the weak force, are not displayed. Figure taken from Ref. [1].

In the Standard Model, there exist three forces: the strong force, the electromagnetic force, and the weak force. The weak force is the weakest of the three, and interaction with the weak force is the only way for a quark to undergo a flavour change to a different generation. Cabibbo was the first to describe the coupling of the weak interaction in the case of two generations in a matrix [2]. Kobayashi and Maskawa later

extended this matrix, which is now known as the CKM-matrix [3]:

$$V_{CKM} = \begin{pmatrix} V_{ud} & V_{us} & V_{ub} \\ V_{cd} & V_{cs} & V_{cb} \\ V_{td} & V_{ts} & V_{td} \end{pmatrix}. \tag{1.1}$$

The CKM-matrix is required to be a unitary matrix. All elements of the CKM matrix have been measured to be consistent with a unitary matrix. However, within errors, it is possible to introduce a fourth family by extending this matrix to a four by four matrix. In addition, the consistency of the CKM framework can be scrutinised by many different measurements of the parameters that describe the unitary CKM matrix. Therefore, it is useful to measure the CKM elements with a higher precision to test unitarity of the CKM-matrix to validate the model and to obtain more information about a potential fourth family, or obtain more insight in the question why there are only three generations.

The unitarity property of the CKM-matrix allows to explore the unitarity relations. One of these unitarity relations is

$$V_{ub}^* V_{ud} + V_{cb}^* V_{cd} + V_{tb}^* V_{td} = 0. \tag{1.2}$$

This relation can be divided by $V_{cb}^* V_{cd}$ to be visualised as a unitarity triangle in the complex plane. Many measurements have been performed on different parameters entering this equation and have been combined by the CKMFitter group into the unitarity triangle as shown in Fig. 1.2 [4]. The dark green band in this figure shows the magnitude of the CKM element V_{ub}. With its large uncertainty, it is the least well-known CKM element. Therefore, it would be very interesting to further investigate $|V_{ub}|$.

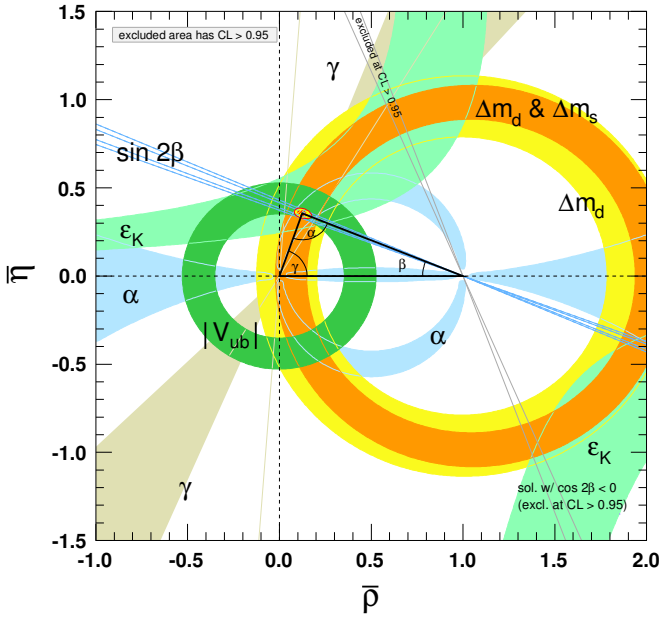

Figure 1.2 – A plot showing the current CKM fit in the imaginary plane. The red dashed area around the triangle's apex is the global combination corresponding to a 68% confidence level. Figure taken from Ref. [5]

Furthermore, on this CKM element, there is currently an unexplained inconsistency between the inclusive and exclusive measurements of $|V_{ub}|$, as shown in Fig. 1.3. The

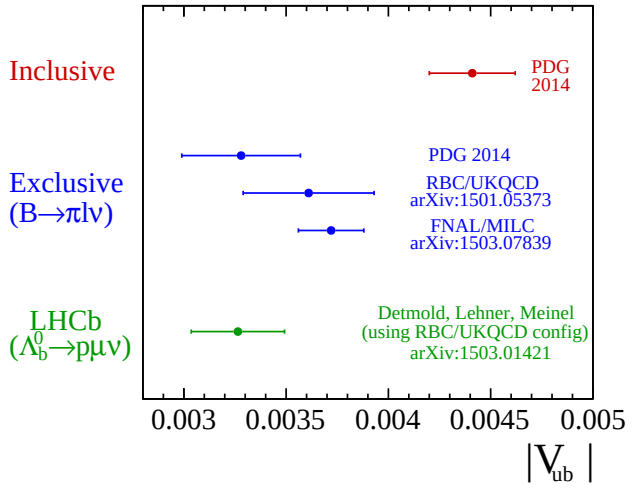

Figure 1.3 – Experimental constraints on $|V_{ub}|$, clearly showing the discrepancy between the inclusive and exclusive measurements. Figure taken from Ref. [6].

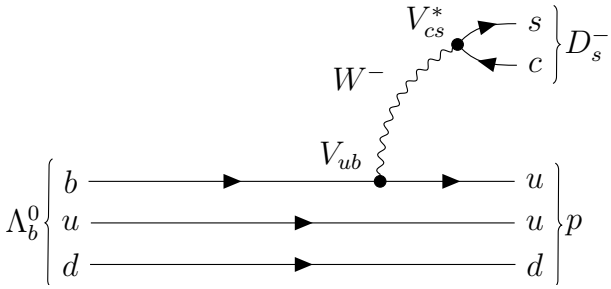

Figure 1.4 – The Feynman diagram of the decay $\Lambda_b^0 \to D_s^- p$.

inclusive measurements performed by the BaBar collaboration using $\overline{B} \to X_u \ell \overline{\nu}_\ell$ gave rise to the average inclusive measurement of $|V_{ub}| = (4.49 \pm 0.15\,^{+0.16}_{-0.17} \pm 0.17) \times 10^{-3}$ [7]. Several exclusive measurements of LHCb [6], Fermilab and MILC [8], and the RBC and UKQCD collaborations [9] have given rise to the average exclusive measurement of $|V_{ub}| = (3.70 \pm 0.10 \pm 0.12) \times 10^{-3}$. A new measurement of an exclusive $|V_{ub}|$ measurement could give more insight in this discrepancy.

Hence it is interesting to investigate the branching ratio of $\Lambda_b^0 \to D_s^- p$, since it is proportional to $|V_{ub}|$, as shown the Feynman diagram of the decay in Fig 1.4. However, it is also proportional to the non-factorizable effect of effective field theory due to the interaction between the involved hadrons by the strong force. The branching ratio of the decay $\Lambda_b^0 \to D_s^- p$ is proportional to:

$$B(\Lambda_b^0 \to D_s^- p) \propto |V_{ub}|^2 \, |a_{NF}|^2 \, f_{D_s^-}^2 F_{\Lambda_b^0 \to p}^2(m_{D_s^-}), \tag{1.3}$$

where $f_{D_s^-}$ is the decay constant of the D_s^- meson and $F_{\Lambda_b^0 \to p}^2(m_{D_s^-})$ is the form factor of the decay Λ_b^0 to p, as a function of the energy of the D_s^- meson. Both the decay constant and form factor are dependent on the strong force. The parameter a_{NF} is the non-factorisable effect that describes gluon interactions between the D_s^- meson and the proton. Unfortunately, it is currently not known how to accurately compute this component. Therefore, until more knowledge on non-factorisable effects is available, we can only obtain a measurement of $|V_{ub}| \times |a_{NF}|$. Furthermore, the decay $\Lambda_b^0 \to D_s^- p$ has not been observed before and only an upper limit of the branching fraction of

4.8×10^{-4} has been set by the LHCb collaboration in 2014 [5, 10]. In addition, this decay is a background to other analyses, like the study of *CP* violation with $B_s^0 \to D_s^- K^+$ decays, where knowledge on the amount of $\Lambda_b^0 \to D_s^- p$ decays is useful. Finally, the non-factorisable effects of the $\Lambda_b^0 \to D_s^- p$ decay can be compared to non-factorisable effects in b-meson decays.

The strategy for obtaining this branching fraction is to determine the yield of the decay $\Lambda_b^0 \to D_s^- p$. We study the specific case where the D_s^- meson decays as $D_s^- \to K^- K^+ \pi^-$. Since we do not know the production rate of the Λ_b^0 baryon, the branching fraction is normalised to the decay $\Lambda_b^0 \to \Lambda_c^+ \pi^-$, with the branching fraction of $(4.9 \pm 0.4)\%$,where the Λ_c^+ baryon decays as $\Lambda_c^+ \to p K^- \pi^+$. We find the branching ratio of $\Lambda_b^0 \to D_s^- p$ according to the equation

$$\frac{B(\Lambda_b^0 \to D_s^- p)}{B(\Lambda_b^0 \to \Lambda_c^+ \pi^-)} = \frac{N(\Lambda_b^0 \to (D_s^- \to K^- K^+ \pi^-) p)}{N(\Lambda_b^0 \to (\Lambda_c^+ \to p K^- \pi^+) \pi^-)} \times \frac{\epsilon(\Lambda_b^0 \to (\Lambda_c^+ \to p K^- \pi^+) \pi^-)}{\epsilon(\Lambda_b^0 \to (D_s^- \to K^- K^+ \pi^-) p)} \times \frac{B(\Lambda_c^+ \to p K^- \pi^+)}{B(D_s^- \to K^- K^+ \pi^-)}, \quad (1.4)$$

where N is the yield for the specific decay, ϵ the detection efficiency of the specific decay, and B the branching fraction of the decay. This normalisation mode is chosen because both decays have a similar topology, with a charmed hadron decaying into three hadrons, accompanied by a so-called companion particle. In this thesis, when a certain decay, such as $\Lambda_b^0 \to D_s^- p$, is mentioned, its charged conjugated decay, $\overline{\Lambda}_b^0 \to D_s^+ \overline{p}$, is also included in this notation. Furthermore, when denoting the decay $\Lambda_b^0 \to D_s^- p$ ($\Lambda_b^0 \to \Lambda_c^+ \pi^-$), it is implied that the D_s^- (Λ_c^+) decays to $K^- K^+ \pi^-$ ($p K^- \pi^+$).

In this thesis, we present the world's first observation of the decay $\Lambda_b^0 \to D_s^- p$. In Chapter 2 we first present a brief description of the LHCb detector and simulation methods. In Chapter 3 the selection criteria for both decay channels, the optimisation to distinguish between signal and combinatorial background, and the selection of protons for the decay $\Lambda_b^0 \to D_s^- p$ is shown. Furthermore, we give the efficiencies of these applied cuts. The fit model is described in Chapter 4 and the signal yields are shown in Chapter 5 for both decays. In Chapter 6 we discuss the studies for the systematic uncertainties to be done for this analysis. To conclude, in Chapter 7 we present the results of this analysis and we conclude this thesis and give an outlook on further research for this decay process in Chapter 8. In addition, a larger selection of background fits as described in Section 3.4.4 is shown in Appendix A and the probability density functions for background templates are shown in Appendix B.

Chapter 2

Detector and Simulation

The Large Hadron Collider (LHC), located at CERN, near Geneva in Switzerland, is the largest particle collider in the world. Protons are accelerated in bunches in several pre-accelerators before they enter the LHC. This synchrotron is a circular tunnel of almost 27 km in circumference and collides protons with a centre-of-mass energy of 13 TeV [11, 12]. The protons are collided at four interaction points. At each of these points, detectors are placed to study the collisions. The four main detectors at these points are:

- ATLAS [13] and CMS [14]. They are the two largest detectors. These detectors are general-purpose detectors used to study a large range of physics phenomena.
- ALICE [15] is a specialised detector used to study the quark-gluon plasma.
- The LHCb detector [16] is specialised to study the difference in behaviour between matter and antimatter by studying CP violation in hadrons containing b or c quarks.

2.1 LHCb Detector

The LHCb detector is built to study CP violation and rare decays in $b-$ and $c-$hadrons [16]. One of the main properties of b and $\overline{b}$ hadrons is that, at high energy, the production occurs a same forward or backward cone along the direction of the beam pipe. Therefore, the LHCb detector is chosen to be a single-arm forward detector, as shown schematically in Fig 2.1. Due to this outlay, the detector covers a pseudorapidity range of $2 \leq \eta \leq 5$, whereas the ATLAS and CMS detectors have a more uniform range for tracking particles. That makes the LHCb detector an excellent detector for studying decay reactions close to the beam pipe. The LHCb detector consists of several sub-detectors, as shown in Fig. 2.1, which are described in Sec. 2.1.1 and 2.1.2.

2.1.1 Tracking

The first important aspect of the LHCb detector is the ability to track particles, in order to determine their line of flight and momentum. Several components in the detector contribute to this. Closest to the beampipe and interaction point is the Vertex Locator (VELO). The VELO is a silicon strip detector placed only 8 mm from the beampipe. Due to this short distance it can identify the displaced secondary vertices of a decay; a characteristic feature of b- and c-hadron decays. The VELO is therefore important for time-dependent measurements. The Silicon Trackers (ST) are placed further downstream in the detector to measure the tracks of the daughter particles of a

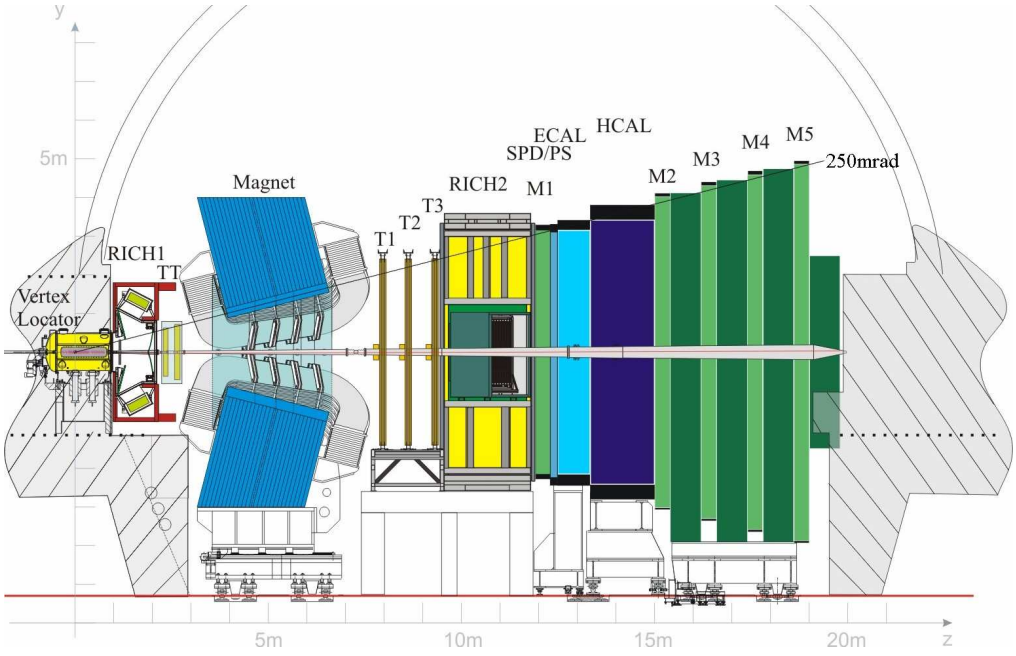

Figure 2.1 – Schematic overview of the LHCb detector. Figure taken from Ref. [16]

decay. The ST consists of the Tracking Turicensis (TT) and the Inner Tracker (IT). The Inner Tracker, together with the Outer Tracker (OT), form the three tracking stations (T1,T2,T3) shown in Fig. 2.1. The ST consists of silicon microstrips, whereas the OT uses straw-tube modules to measure tracks. The magnet in between the tracking stations has an integrated field strength of 4 Tm. Combining all these components, the detector is capable of a momentum resolution of 0.5% for particles with a momentum below 20 GeV/c and 0.8% around 100 GeV/c [17]. The magnet is also able switch to polarity, ensuring that there is no bias in a certain polarity. These polarities are noted as *MagUp* and *MagDown*.

2.1.2 Particle Identification

The second important aspect of the LHCb detector is the ability to identify particles. There are several components in the detector contributing to this. Firstly, the two Ring Imaging CHerenkov Counters (RICH1-2) detect the Cherenkov radiation emitted by a charged particle passing through the detector material. The RICH1 consists out of silica aerogel and C_4F_{10} gas detectors, whereas the RICH2 exists of CF_4 gas radiator. The angle of the produced radiation, with respect to the particle line of flight, is directly related to the speed of the particle. The RICHes can therefore, together with a momentum measurement, distinguish between different decay products such as the pions, kaons and protons. This subdetector provides crucial information to select the $\Lambda_b^0 \to D_s^- p$ decays studied in this thesis.

The Electromagnetic and Hadronic Calorimeters (ECAL and HCAL) are responsible for energy measurements of photons, electrons, and hadrons. The ECAL records the energy deposit of electrons and photons, whereas the HCAL records the energy deposit of charged and neutral hadrons. The information of the calorimeters is used to select $\Lambda_b^0 \to D_s^- p$ decays at the lowest trigger levels. Lastly, the muon system measures the momentum of muons. This stage is effective at detecting muons, since nearly all other particles are absorbed by the ECAL or HCAL before reaching the muon stations.

To quantify the measurements of these stations, each reconstructed charged particle in LHCb is assigned a likelihood of being a kaon, pion or proton. There are two different methods for this measurement, called DLL and ProbNN. The difference in log-likelihood for a kaon or proton with respect to a pion is called respectively $\mathrm{DLL}_{K\pi}$ or $\mathrm{DLL}_{p\pi}$ in this thesis. ProbNN is obtained from a neural network training procedure. This variable has the advantage that it can distinguish a proton in comparison to all other particles instead of only comparing it to the probability of being one other type.

2.2 Simulation

A dedicated Monte Carlo (MC) simulation is used to obtain the shapes of the invariant mass distributions for background processes and signal shape parametrisation. The simulated sample is also used to determine the selection efficiency of the final signal sample. In these simulations, pp collisions are simulated by Pythia [18,19]. The decays of the hadrons are then described by EvtGen [20] where the final-state radiation is generated by Photos [21]. The interaction between the final-state particles and the response of the detector is simulated by Geant4 [22, 23] using the specific LHCb configuration from Gauss [24,25]. Due to the lack of simulation at the time of writing, the Run 2 event simulation of the decay $\Lambda_b^0 \to D_s^- p$ is produced using `RapidSim`, where the pp collision from Pythia was re-used a thousand times, to increase the simulation speed for this decay. Furthermore, the background templates for all Run 2 background samples of the $\Lambda_b^0 \to \Lambda_c^+ \pi^-$ decay are simulated using `RapidSim`. A list of all simulation samples is shown in Table 2.1.

Decay channel	Background	Run 1	Run 2
$\Lambda_b^0 \to D_s^- p$	$\Lambda_b^0 \to D_s^- p$	Official 2012	`RapidSim` 2015,2016
	$\Lambda_b^0 \to D_s^{*-} p$	Official 2012	Official 2012
	$B_s^0 \to D_s^- \pi^+$	Official 2012	Official 2015,2016 `TISTOS`
	$B_s^0 \to D_s^{*-} \pi^+$	Official 2012	Official 2015 `TISTOS`
	$B_s^0 \to D_s^- \rho^+$	Official 2012	Official 2015,2016 `TISTOS`
	$B_s^0 \to D_s^- K^+$	Official 2012	Official 2015 `TISTOS`
	$B_s^0 \to D_s^{*-} K^+$	Official 2012	Official 2012
	$B_s^0 \to D_s^- K^{*+}$	Official 2012	Official 2012
$\Lambda_b^0 \to \Lambda_c^+ \pi^-$	$\Lambda_b^0 \to \Lambda_c^+ \pi^-$	Official 2012	Official 2015,2016
	$\Lambda_b^0 \to \Lambda_c^+ K^-$	Official 2012	`RapidSim` 2016
	$\Lambda_b^0 \to \Lambda_c^+ \rho^-$	`RapidSim` 2016	`RapidSim` 2016
	$\Lambda_b^0 \to \Sigma_c^+ \pi^-$	`RapidSim` 2016	`RapidSim` 2016
	$B^0 \to D^- \pi^+$	Official 2012	`RapidSim` 2016
	$B_s^0 \to D_s^- \pi^+$	Official 2012	`RapidSim` 2016

Table 2.1 – List of all simulation samples used for the decay channels $\Lambda_b^0 \to D_s^- p$ and $\Lambda_b^0 \to \Lambda_c^+ \pi^-$. The years indicate the specific configuration used for that year. Some samples are produced using `RapidSim`, as described in Sec. 2.2. Some official samples are label with `TISTOS`. These official samples have a bug in the TISTOS configuration, this effect for the background templates, as described in Sec. 4.1.1, is negligible.

Chapter 3

Dataflow, Selection, and Efficiencies

The protons circulating in the LHC provide 40 million proton-proton collisions at LHCb every second. This produces a vast amount of data of about 1 Tbytes per second. Therefore, there are a lot of selection steps at multiple levels. The first is the trigger selection, which provides a rough selection described in Sec. 3.1. The next step is the reconstruction and stripping selection, where tracks are reconstructed and events are selected based on kinematic properties as described in Sec. 3.2 and optimised in Sec. 3.4. After this, the analysis specific-selections are described in Sec. 3.3 and the efficiencies in Sec. 3.5.

The LHC has been running since 2010 for six years with a pause in 2013 and 2014. The two different time periods before and after the pause of data taking are referred to as Run 1 and Run 2. In this thesis, we use the 2011 and 2012 data from Run 1 and the 2015 and 2016 data from Run 2. In Run 1 the LHC collided protons with a centre of mass energy of 7 TeV in 2011 and 8 TeV in 2012. In Run 2, the LHC was able to increase the centre of mass energy to 13 TeV in both years [26]. The differences in collision energy, but also differences in data-processing, are the cause of differences in detection efficiencies between Run 1 and Run 2. Therefore, we study the two runs separate. The recorded luminosity of both runs for the different magnet polarities are shown in Table 3.1.

	Run 1		Run2	
	$\int \mathcal{L}\ (2011)/\,\mathrm{fb}^{-1}$	$\int \mathcal{L}\ (2012)/\,\mathrm{fb}^{-1}$	$\int \mathcal{L}\ (2015)/\,\mathrm{fb}^{-1}$	$\int \mathcal{L}\ (2016)/\,\mathrm{fb}^{-1}$
MagUp	0.42	0.9988	0.1476	0.7992
MagDown	0.56	0.9912	0.1804	0.8658

Table 3.1 – The recorded integrated luminosity of LHCb in several years.

In this chapter we first discuss the trigger selection and stripping selection in Sec. 3.1 and Sec. 3.2 respectively. We then discuss the analysis specific selection in Sec. 3.3 and optimize the BDT and ProbNN$_p$ in Sec. 3.4. Lastly, the efficiencies of these selection criteria are discussed in Sec. 3.5.

3.1 Trigger Selection

The trigger selection consists of several levels, which all occur online [27]. The first level, called Level-0 (L0), ensures that the data frequency of 40 MHz goes down to 1 MHz [28]. Due to the large mass of the b-hadrons, the produced daughter particles often have a large transverse momentum and energy. Therefore, the L0 trigger can use this characteristic to only select decays that have deposited a lot of energy in the ECAL or HCAL or contain high momentum muon candidates in the muon chambers [16,29,30].

The software trigger, also called the High Level Trigger (HLT), is split into two levels. In this stage, a minimal reconstruction of the tracks is performed. The HLT1 processes information provided by the VELO to check that a particular candidate has had a long flight time as this is a characteristic of the b-hadrons. Furthermore, it is required that at least one track in the event has a momentum of at least 1.7 GeV/c and an χ^2_{IP} with respect to a primary interaction point greater than 16, where the χ^2_{IP} is defined as the difference in χ^2 of the primary interaction point with and without the considered particle track. After the HLT1 the data flow is reduced to approximately 100 kHz [16, 29–31]. In this analysis, we require for the Run 1 sample that the HLT1 has confirmed the L0 trigger. For events in the Run 2 sample we require that HLT1 was triggered globally or it found one or two valid tracks.

At 100 kHz, the data rate is low enough for a full reconstruction of the tracks in the HLT2. For each track is required that its transverse momentum is higher than 300 MeV/c and it is required that there is a two-, three-, or four- track vertex constructed out of the tracks. The HLT2 also finds characteristic resonant decay modes such $\phi \to K^+K^-$. After this final online selection, the information is stored at an approximated rate of 5 kHz after which it will be stored and fully reconstructed offline [16, 29, 30]. For both runs, we require that HLT2 was able to construct a two-, three- or four- track vertex out of the tracks. For the $\Lambda_b^0 \to D_s^- p$ candidates we also accept the candidate if the HLT2 was triggered on a $\phi \to K^+K^-$ decay. In Run 2, the performance of HLT2 has been drastically improved, such that it is now possible to fully reconstruct the events online [32].

3.2 Stripping Selection

The next step is the so-called stripping, where the events are reconstructed and cuts are made based on kinematic properties. There are two stripping lines used, the $B^0 \to D^-\pi^+$ stripping line for the $\Lambda_b^0 \to D_s^- p$ sample[1] and one for the $\Lambda_b^0 \to \Lambda_c^+\pi^-$ sample[2]. Both stripping lines are contained in the `Stripping21(r1)` for 2012(2011) and `Stripping24` and `Stripping28` for 2015 and 2016, respectively. A key feature of these stripping lines is that they are only based on kinematic and geometric cuts and do not contain any particle identification cuts. In the $B^0 \to D^-\pi^+$ stripping line there are first some loose kinematic cuts. After this, a $D_s^\mp$ is constructed out of three light hadrons. This $D_s^\mp$ candidate is then combined with the companion hadron $h^\pm$ to for our b hadron candidate. A more detailed description of this stripping line can be found in Ref. [33]. The $\Lambda_b^0 \to \Lambda_c^+\pi^-$ stripping line first builds the $\Lambda_c^\pm$ from a proton, kaon and pion candidate, after which it combines the $\Lambda_c^\pm$ candidate with a pion to form the Λ_b^0 candidate. More information on this stripping line can be found in Ref. [34].

[1] B02DPiD2HHHBeauty2CharmLine. This stripping line constructs both the decay $B^0 \to (D^- \to K^+\pi^-\pi^-)\pi^+$ and the $B_s^0 \to (D_s^- \to K^-K^+\pi^-)\pi^+$ decay.

[2] Lb2LcPiLc2PKPiBeauty2CharmLine

3.3 Analysis Selection

In addition to the stripping selection, we apply several cuts to eliminate background processes. There are requirements based on kinematic variables (such as momentum, lifetime and invariant mass) and particle identification (PID), as described in Sec 2.1.2. Below we specify each of these cuts for the $\Lambda_b^0 \to D_s^- p$ and $\Lambda_b^0 \to \Lambda_c^+ \pi^-$ decays. A summary of these selection criteria is shown in Table 3.2.

3.3.1 Analysis Selection for $\Lambda_b^0 \to D_s^- p$

First, we apply a mass constraint around the D_s^- mass, where we require that the mass of the D_s^- candidate must lie within $[1950, 1990]\,\text{MeV}/c^2$, closely around the D_s^- mass of $1968\,\text{MeV}/c^2$ [5]. We also require that the χ^2 of the vertex separation between the Λ_b^0 candidate and D_s^- candidate is at least 2, to eliminate the process $\Lambda_b^0 \to pK^-K^+\pi^-$. Since the candidates where the reconstructed lifetime of the D_s^- is smaller than zero are likely to be combinatorial background, we require that the decay time of the D_s^- candidate is larger than zero. For low momenta of the proton candidate, it is difficult to distinguish between protons and kaons. Therefore, we also require that the momentum of the proton candidate is at least $10\,\text{GeV}/c$ and the transverse momentum to be at least $400\,\text{MeV}/c$. Lastly, we apply a strict requirement on the proton ProbNN_p, which will be further explained and optimised in Sec. 3.4.

In order to obtain a clean D_s^- signal, we apply veto's to eliminate the decays $D^+ \to K^-\pi^+\pi^+$ and $\Lambda_c^+ \to pK^-\pi^+$, where one of the daughter particles of the D_s^- candidate is misidentified. For the D^+ veto, we reject candidates if the mass of the D_s^- candidate, in the D^+ mass hypothesis, falls inside the region $[1840, 1940]\,\text{MeV}/c^2$, unless the $\text{DLL}_{K\pi}$ of the K^- is higher than 10. For the Λ_c^+ veto, we reject candidates where the D_s^- candidate, in the Λ_c^+ mass hypothesis, falls in the range $[2255, 2315]\,\text{MeV}/c^2$, unless the K^- satisfies $\text{DLL}_{K\pi}$-$\text{DLL}_{p\pi} > 5$ and $\text{DLL}_{p\pi} < 0$. We also apply a veto for the process $D^0 \to K^+K^-$, which can be identified as a D_s^- candidate if a random π is combined with the two kaons. For this veto we require that the invariant mass of the kaon pair is below $1840\,\text{MeV}/c^2$.

Lastly, we split our sample according to three decay modes of the D_s^-: $D_s^- \to (\phi \to K^+K^-)\pi^-$, $D_s^- \to (K^{*0} \to K^+\pi^-)K^-$, and the non-resonant mode $D_s^- \to K^-K^+\pi^-$. For the $\phi\pi^-$-mode we require that the invariant mass of the two kaons lies in the range $[1000, 1040]\,\text{MeV}/c^2$, close to the known ϕ mass of $1019\,\text{MeV}/c^2$ [5]. Furthermore, we require in this case that the $\text{DLL}_{K\pi}$ of both kaons must be above -2. If the invariant mass of the $K^-\pi^+$ pair falls in the range $[842, 942]\,\text{MeV}/c^2$ we classify the decay as the $K^{*0}K^-$-mode if the $\text{DLL}_{K\pi}$ of the K^+ is be above -2, whereas the $\text{DLL}_{K\pi}$ of the K^- must be above 5. If the decay particles of the D_s^- candidate do not fulfil these requirements, the decay is classified as non-resonant if the $\text{DLL}_{K\pi}$ of both kaons exceeds 5 and the $\text{DLL}_{K\pi}$ of the pion is smaller than 10.

Since the final state decay $\Lambda_b^0 \to D_s^- p$ is similar to $B_s^0 \to D_s^- \pi^+$ we use the same BDT algorithm. In previous analyses, a $B_s^0 \to D_s^- \pi^+$ data sample was used to find discriminating features between the combinatorial background and the $B_s^0 \to D_s^- \pi^+$ signal. This was done using a Boosted Decision Tree (BDT). This BDT is trained on $B_s^0 \to D_s^- \pi^+$ data from the full Run 1 dataset, using the stripping `Stripping 21(r1)` and some basic kinematic and PID cuts to provide a clean sample. The upper tail (above $5445\,\text{MeV}/c^2$) of $m(D_s^\mp h^\pm)$ is used to represent the combinatorial background [33]. The

BDT algorithm is based on several kinematic properties of the decay such as the quality of the displaced decay vertex from the primary vertex. In this analysis, this BDT algorithm is used for Run 1 and Run 2 and we apply a fairly strict cut on the BDT, which is optimised as described in Sec. 3.4.

3.3.2 Analysis Selection for $\Lambda_b^0 \to \Lambda_c^+ \pi^-$

For the $\Lambda_b^0 \to \Lambda_c^+ \pi^-$ decay we use a strict mass cut around the invariant mass of the Λ_c^+ of $2286\,\mathrm{MeV}/c^2$ [5], where we require that the invariant mass lies in the range $[2270, 2302]\,\mathrm{MeV}/c^2$. Furthermore, we also require that the reconstructed Λ_c^+ decay time exceeds zero. For the companion pion we require a minimum momentum of $10\,\mathrm{GeV}/c$, and the $\mathrm{DLL}_{K\pi}$ of the pion must be at most 0. For the daughter particles of the Λ_c^+ we require that the $\mathrm{DLL}_{K\pi}$ of the kaon must be at least 0, the $\mathrm{DLL}_{K\pi}$ of the pion must be at most 5, and the ProbNN_p of the proton must be at least 0.6. The BDT cut for Run 2 must be at least 0.4 , whereas for Run 1 is should exceed -0.5, to improve the fit stability.

Applied to	Description	Requirement
All decays	Momentum of companion particle	$> 10\,\text{GeV}/c$
	Transverse momentum of companion particle	$> 400\,\text{MeV}/c$
	Number of tracks in event	> 15 and < 1000
$\Lambda_b^0 \to D_s^- p$		
	D_s^- mass	$\in [1950, 1990]$ MeV/c^2
	D_s^- lifetime	> 0
	D_s^- vertex separation χ^2 (wrt. Λ_b^0 vertex)	> 2
	Run 1 ProbNN$_p$ of p	> 0.7
	Run 2 ProbNN$_p$ of p	> 0.9
	BDT	> 0.4
$D_s^- \to K^- K^+ \pi^-$		
	D^0 veto:	
	$m(K^+K^-)$	< 1840 MeV/c^2
	D^+ veto:	
	DLL$_{K\pi}$ of K^-	> 10, or
	D_s under D hypothesis	$\notin [1840, 1940]$ MeV/c^2
	Λ_c^+ veto:	
	p veto of K^-	(DLL$_{K\pi}$-DLL$_{p\pi} > 5$ and DLL$_{p\pi} < 0$), or
	D_s^- under Λ_c^+ hypothesis	$\notin [2255, 2315]$ MeV/c^2
$D_s^- \to \phi\pi^-$		
	$m(K^+K^-)$	$\in [1000, 1040]$ MeV/c^2, and
	DLL$_{K\pi}$ of both K	> -2
$D_s^- \to K^{*0}\, K^-$		
	$m(\pi^-K^+)$	$\in [842, 942]$ MeV/c^2, and
	DLL$_{K\pi}$ of K^-	> 5, and
	DLL$_{K\pi}$ of K^+	> -2
$D_s^- \to (K^-K^+\pi^-)_{\text{nonres}}$		
	DLL$_{K\pi}$ of both $K^\pm$	> 5, and
	DLL$_{K\pi}$ of π^-	< 10
$\Lambda_b^0 \to \Lambda_c^+ \pi^-$		
	DLL$_{K\pi}$ of π^-	< 0
	Λ_c^+ mass	$\in [2270, 2302]\,\text{MeV}/c^2$
	Λ_c^+ lifetime	> 0
	Run 1 BDT	> -0.5
	Run 2 BDT	> 0.4
$\Lambda_c^+ \to pK^-\pi^+$		
	ProbNN$_p$ of p	> 0.6
	DLL$_{K\pi}$ of K^-	> 0
	DLL$_{K\pi}$ of π^-	< 5

Table 3.2 – Summary of selection criteria for the decay channels $\Lambda_b^0 \to D_s^- p$ and $\Lambda_b^0 \to \Lambda_c^+ \pi^-$.

3.4 BDT and ProbNN$_p$ Optimisation

3.4.1 Strategy

We simultaneously determine the optimal cut value for the BDT, to reduce the combinatorial background, and the ProbNN$_p$ cut for the companion proton, to reduce background from the decays $B_s^0 \to D_s^{-(*)}(\pi^+, \rho^+)$ and $B_s^0 \to D_s^{-(*)}K^{+(*)}$. To find the optimal cut value for these two variables we use the optimisation expression [35]:

$$f_{\text{Punzi}} = \frac{\epsilon(\text{BDT}, \text{ProbNN}_p)}{a/2 + \sqrt{B(\text{BDT}, \text{ProbNN}_p)}}, \tag{3.1}$$

where ϵ is the efficiency of the combined cuts, B is the absolute expected background yield under the signal peak with the applied cuts and a the desired significance in units of the number of standard deviations. We study $a = 10$ and $a = 15$. To optimise this expression as a function of the BDT and ProbNN$_p$ cut, we need an efficiency for the signal yield and an estimate of the background yield for each pair of cut values. We scan the full range of the BDT ($[-1, 1]$) with a step size of $\Delta\text{BDT} = 0.05$, as well as the full range of the ProbNN$_p$ values ($[0, 1]$) with a step size of $\Delta\text{ProbNN}_p = 0.05$.

3.4.2 BDT Efficiency

The BDT is described in Sec. 3.3.1. The BDT is dependent on kinematic variables, which are well-modelled in simulation. Therefore, we obtain the efficiency directly from MC. We also study the background retention by studying the upper tail of the signal peak $m(pD_s^-) > 6000\,\text{MeV}/c^2$, which consists only of combinatorial background due to the large mass of the Λ_b^0 baryon. These distributions are shown for Run 1 and Run 2 data in Fig. 3.1.

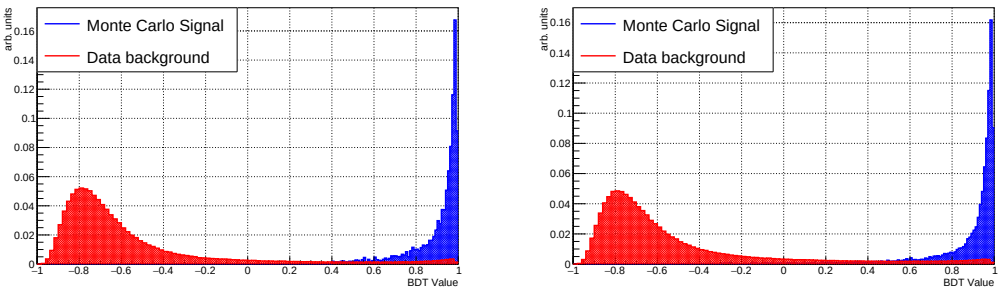

(a) Run 1 **(b)** Run 2

Figure 3.1 – The distribution of BDT values for simulation signal (red) and combinatorial background from data (blue) for Run 1 and Run 2 for the sample $\Lambda_b^0 \to D_s^- p$.

3.4.3 ProbNN$_p$ Efficiency

According to Ref [36], PID variables in simulation only give approximate values, and can therefore not be used for efficiency calculations. The unsatisfactory comparison of PID variables in data and simulation is shown using a sample of $\Lambda_b^0 \to (\Lambda_c^+ \to pK^-\pi^+)\pi^-$ decays. To obtain a background-subtracted data sample, we use a tool called *sPlot* [37]. First, we perform a fit to the decay $\Lambda_c^+ \to pK^-\pi^+$, where we describe the background by a linear function and the signal as the sum of two Gaussian distributions. This fit is shown in Fig. 3.2. The *sPlot* tool is then able to extract weights for each Λ_b^0 candidate, called *sWeights*. After obtaining these *sWeights*, we plot the *sWeighted* ProbNN$_p$ distributions and compare this to the distributions from simulation. This

comparison is shown in Fig. 3.3, where we see that the distributions do not match. We conclude that we can not use the efficiency directly from MC and therefore have to use another method.

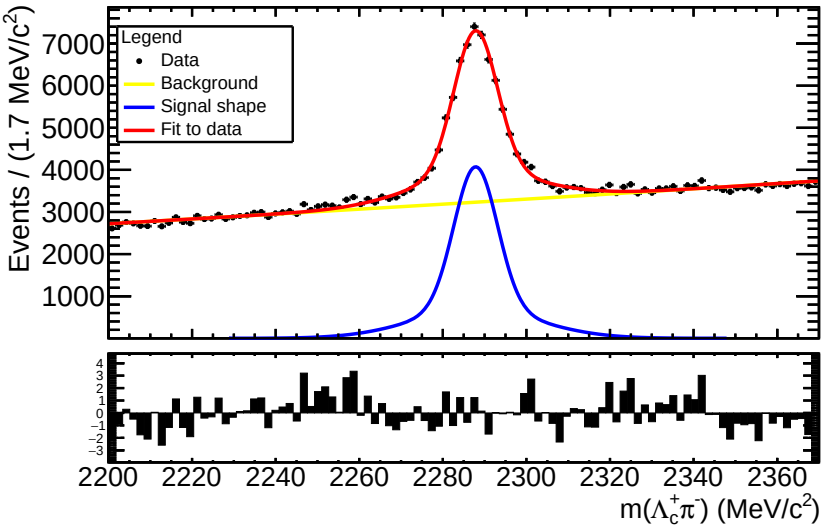

Figure 3.2 – The *sPlot* of the decay $\Lambda_c^+ \to pK^-\pi^+$.

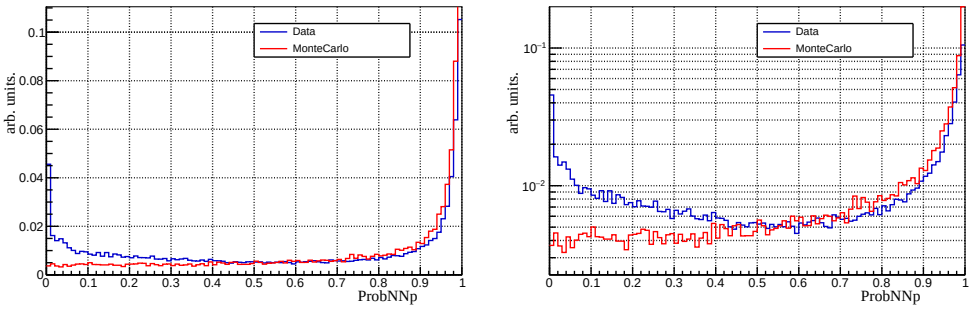

(a) Proton

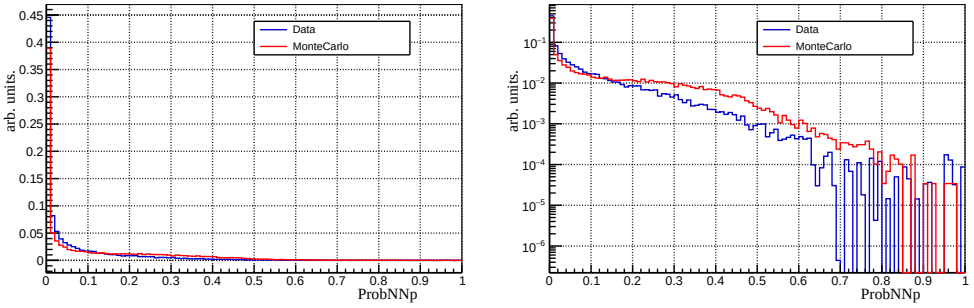

(b) Kaon

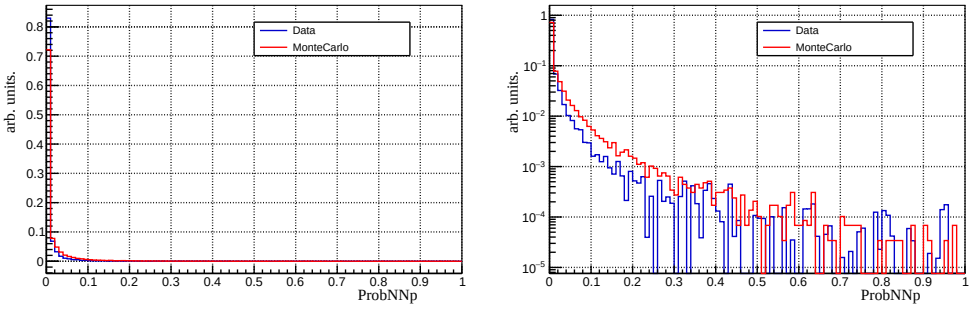

(c) Pion

Figure 3.3 – The ProbNN$_p$ distributions of the decay products of $\Lambda_c^+ \to pK^-\pi^+$. The *sWeighted* data is shown in blue, whereas the simulation is shown in red. On the left the distributions are shown in linear scale, whereas on the right they are shown in logarithmic scale. For high ProbNN$_p$ values for the kaon and pion, we see high fluctuations, these are due to low statistics in these regions.

Instead, we use an LHCb software package called `PIDCalib` [36]. This package uses a clean sample of protons from *sWeighted* data and computes the efficiency of a PID cut in bins of number of tracks in the event (nTracks) and momentum (p). There are two available calibration samples. The first is from the $\Lambda^0 \to p\pi^-$ decay and is high in statistics; however, the proton momenta in this decay are too low in comparison with $\Lambda_b^0 \to D_s^- p$ companion protons. The second sample is from $\Lambda_c^+ \to pK^-\pi^+$ decays, which is only available for Run 1 and much lower in statistics, but covers the appropriate momentum spectrum. Therefore, we will use this second sample for Run 1 to compute the efficiency of the ProbNN$_p$ cut on our companion proton, and the $\Lambda^0 \to p\pi^-$ sample to compute the efficiencies in Run 2.

3.4.4 Background yield

In order to find the optimal cut value using Eqn. 3.1, we also need an estimate of the background yield for each pair of cut values. In order to do this, we fit the background around the expected signal peak in data. For this background fit we only take the

mass range $m_{D_s^- p} \in [5500, 5560] \cup [5680, 6000]$, since we expect our signal peak in the range $m_{D_s^- p} \in [5580, 5660]$. To make the fit of the background components around our signal peak we take the sum of two exponential functions: one for the combinatorial background, and one to account for the upper tail of the $B_s^0 \to D_s^- \pi^+$ peak. We see this structure more clearly for various BDT and ProbNN$_p$ cuts in Fig 3.4 for the Run 1 sample and in Fig. 3.5 for the Run 2 sample. An extended selection of these fits is shown in Appendix A. To estimate the background underneath the signal peak we take the integral in the mass range $m_{pD_s^-} \in [5580, 5660]$.

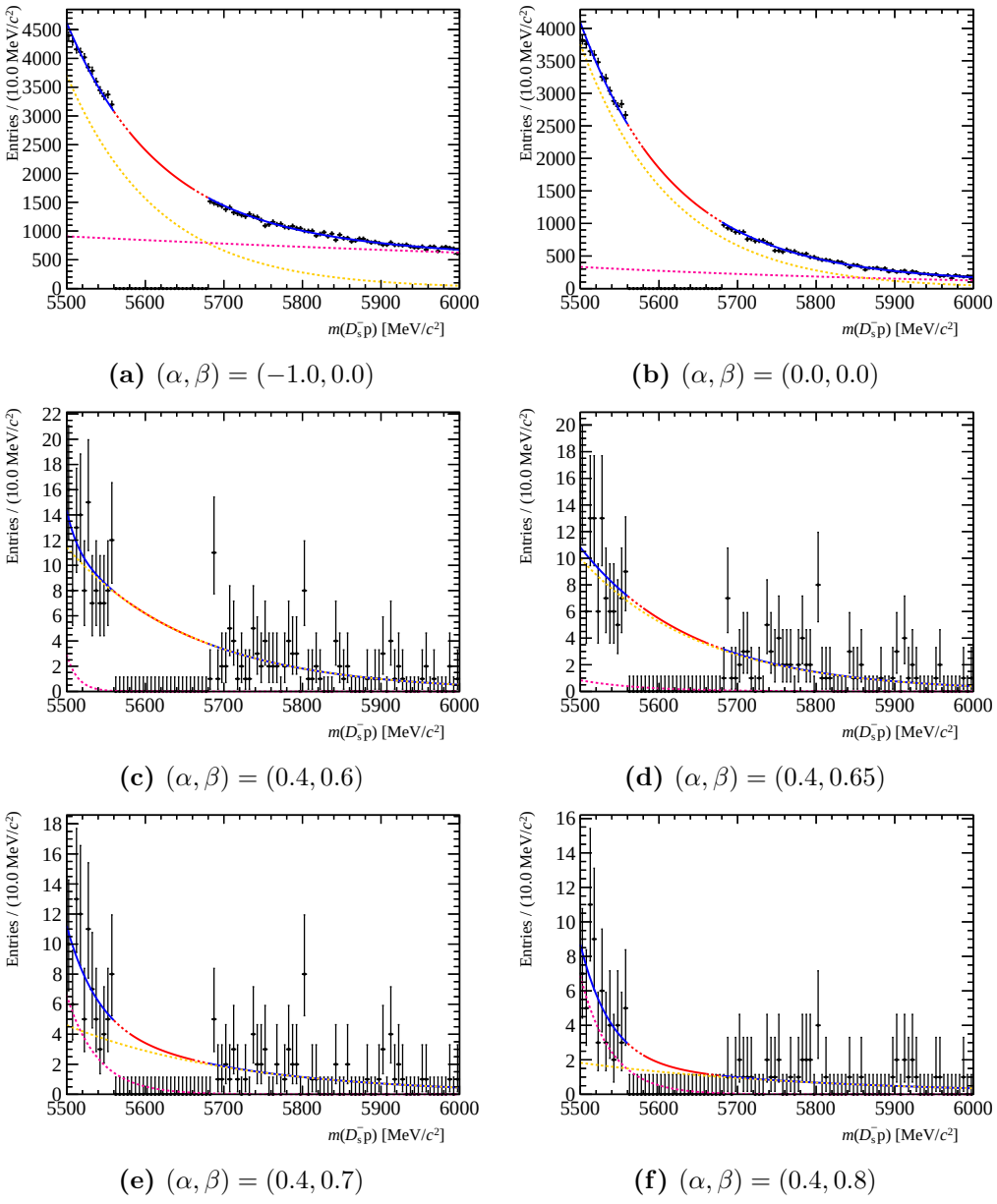

(a) $(\alpha, \beta) = (-1.0, 0.0)$ **(b)** $(\alpha, \beta) = (0.0, 0.0)$

(c) $(\alpha, \beta) = (0.4, 0.6)$ **(d)** $(\alpha, \beta) = (0.4, 0.65)$

(e) $(\alpha, \beta) = (0.4, 0.7)$ **(f)** $(\alpha, \beta) = (0.4, 0.8)$

Figure 3.4 – Several example fits to the $m(D_s^- p)$ distribution, as described in Sec. 3.4.4 for the Run 1 sample, where we fit the background around the peak with two exponential functions. The cuts BDT $> \alpha$ and ProbNN$_p > \beta$ for each figure are defined as (α, β). These values for these fits are chosen to lie close to the chosen cut values for ProbNN$_p$ and BDT in Run 1. The fit is produced excluding the mass-range $m_{D_s^- p} \in [5560, 5680]$, e.g. the area of the solid and dashed red line, and the data points in this region are set to zero. The pink and yellow dashed lines are the two exponential functions that describe the background. The red solid line is used to compute the number of background events under the signal peak. The red dashed line is used in neither the fit nor the computation of the background yield.

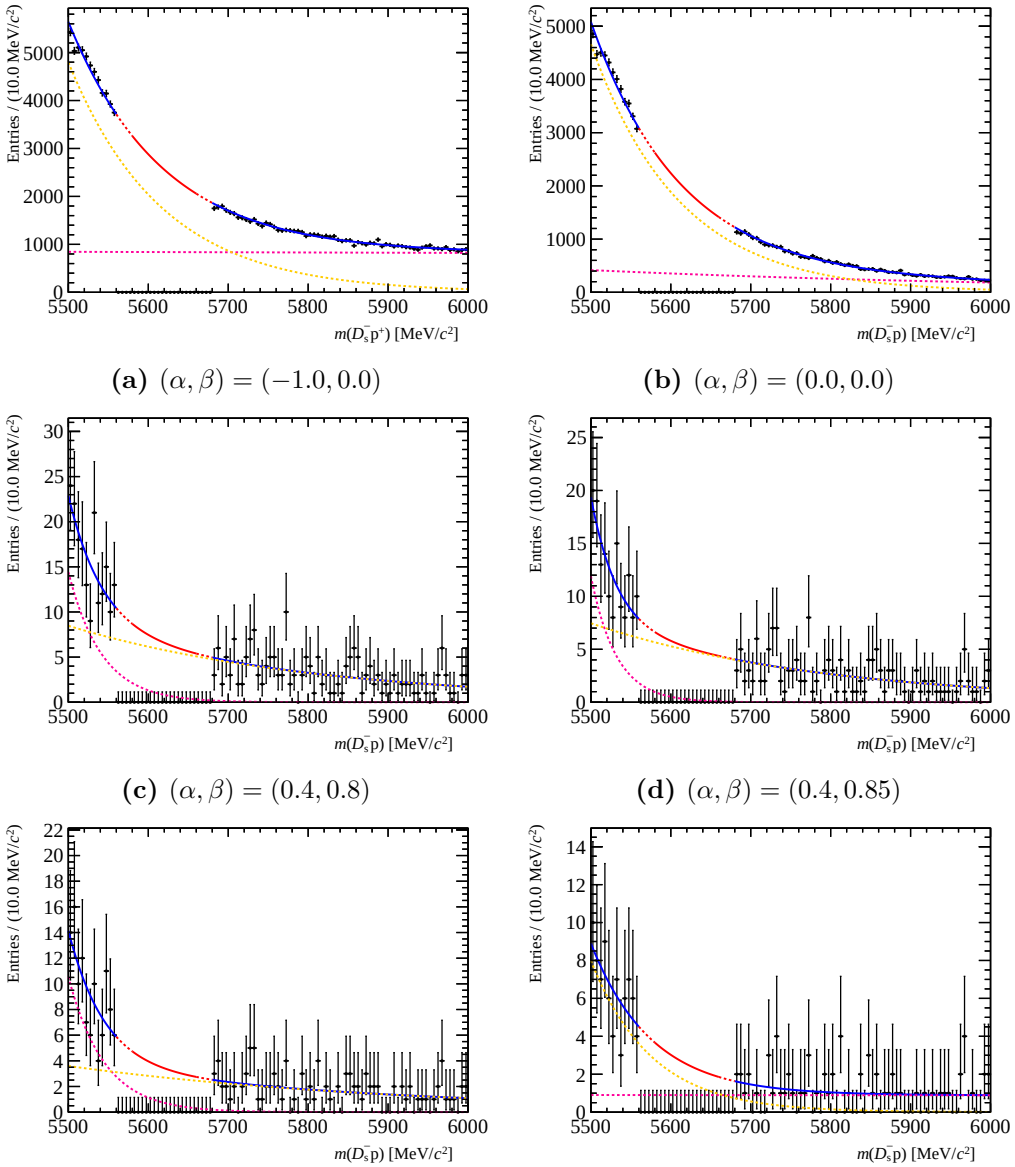

(a) $(\alpha, \beta) = (-1.0, 0.0)$ **(b)** $(\alpha, \beta) = (0.0, 0.0)$

(c) $(\alpha, \beta) = (0.4, 0.8)$ **(d)** $(\alpha, \beta) = (0.4, 0.85)$

(e) $(\alpha, \beta) = (0.4, 0.9)$ **(f)** $(\alpha, \beta) = (0.4, 0.95)$

Figure 3.5 – Several example fits to the $m(D_s^- p)$ distribution, as described in Sec. 3.4.4 for the Run 2 sample, where we fit the background around the peak with two exponential functions. The cuts BDT $> \alpha$ and ProbNN$_p > \beta$ for each figure are defined as (α, β). These values for these fits are chosen to lie close to the chosen cut values for ProbNN$_p$ and BDT in Run 2. The fits are produced using the idental method as in Fig. 3.4.

3.4.5 Punzi Efficiency

Combining the results for the ProbNN$_p$ and BDT efficiencies with the background yield, we compute the Punzi efficiency according to Eq. 3.1 separately for Run 1 and Run 2. In Fig. 3.6 the results for Run 1 are shown. For $a = 10$, we find an optimal point of BDT > 0.4 and ProbNN$_p > 0.7$ (cf. Fig. 3.6a). However, the plateau around the maximum is quite unstable. Therefore, we also study the case where $a = 15$, as shown in Fig. 3.6b. Here we see a well-formed plateau around a maximum of BDT > 0.4 and ProbNN$_p > 0.7$. Both values of a show a maximum at the same cut values, therefore we choose BDT > 0.4 and ProbNN$_p > 0.7$ for the Run 1 sample.
The results for the Run 2 sample are shown in Fig 3.7. We observe for $a = 10$ (cf. Fig. 3.7a) a clear plateau around BDT > 0.4 and ProbNN$_p > 0.9$. For $a = 15$ (Fig. 3.7b) the maximum is at the same place, with a clear plateau around it. Therefore, for Run 2, we choose the cut values BDT > 0.4 and ProbNN$_p > 0.9$.

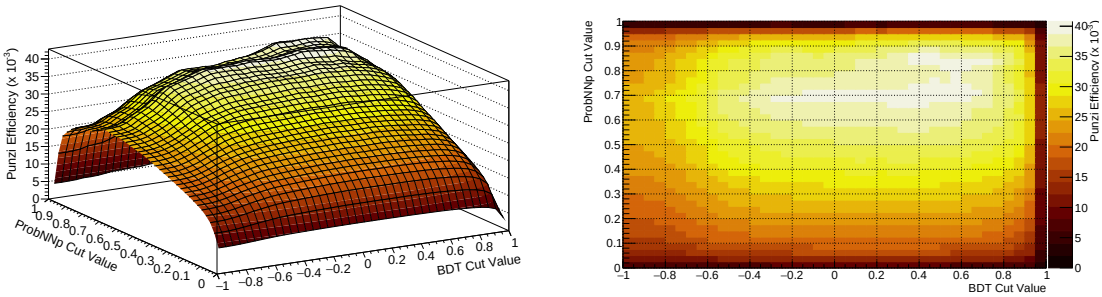

(a) $a = 10$

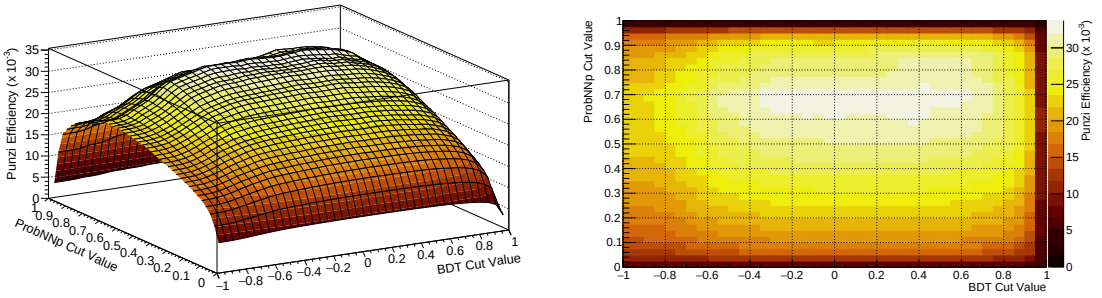

(b) $a = 15$

Figure 3.6 – The Punzi efficiency for the Run 1 sample in two dimensions, BDT and ProbNN$_p$, for $a = 10$ and $a = 15$.

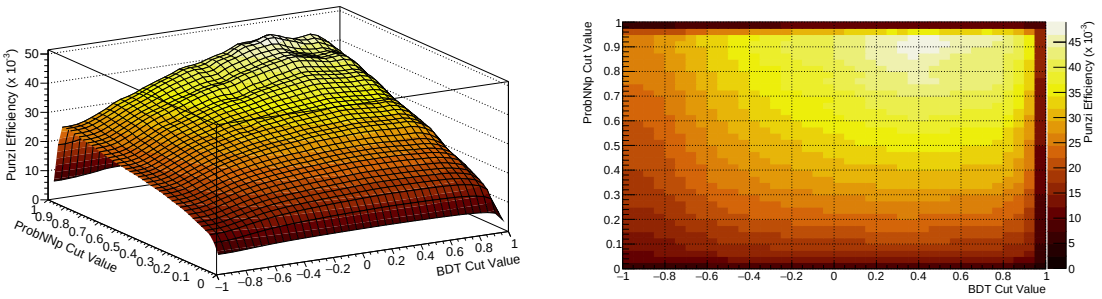

(a) $a = 10$

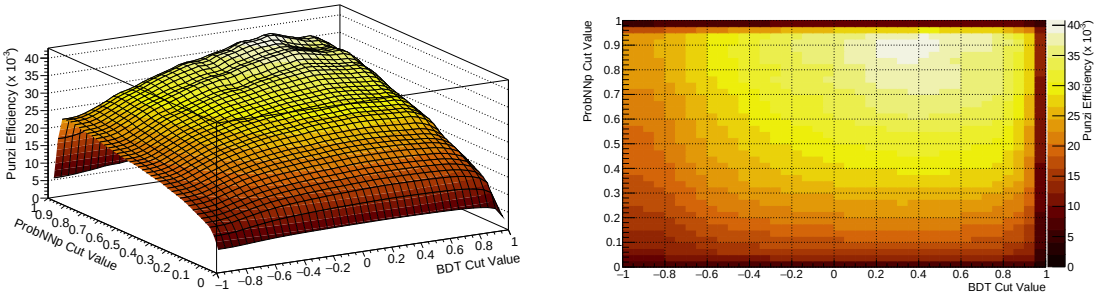

(b) $a = 15$

Figure 3.7 – The Punzi efficiency for the Run 2 sample in two dimensions, BDT and ProbNN$_p$, for $a = 10$ and $a = 15$.

3.5 Selection Efficiencies

In order to obtain the yield of the two decays to calculate the branching ratio, one has to take the reconstruction and selection efficiencies into account. All kinematic efficiencies have been calculated from the corresponding simulation sample as described in Sec. 2.2. The PID cut efficiencies have been calculated using `PIDCalib` as described in Sec. 3.4.3. The efficiencies for the decays $\Lambda_b^0 \to D_s^- p$ and $\Lambda_b^0 \to \Lambda_c^+ \pi^-$ can be found in Table 3.3 and 3.4, respectively.

	Run 1		Run2	
	$\epsilon_{\text{rel}}(\%)$	$\epsilon_{\text{cum}}(\%)$	$\epsilon_{\text{rel}}(\%)$	$\epsilon_{\text{cum}}(\%)$
Generator level and Trigger	18.269 ± 0.04700	18.2690 ± 0.0470	17.9574 ± 0.0059	17.9574 ± 0.0059
Reconstruction & Stripping	3.208 ± 0.0001	0.5861 ± 0.0024	4.139 ± 0.009	0.7432 ± 0.0017
L0, HLT1, HLT2 cuts	93.5216 ± 0.0563	0.5481 ± 0.0022	95.4745 ± 0.0348	0.7096 ± 0.0017
Proton (transverse) momentum	97.4647 ± 0.0368	0.5342 ± 0.0022	97.2057 ± 0.0281	0.6897 ± 0.0017
D_s^- Mass window cuts	95.5437 ± 0.0491	0.5104 ± 0.0021	94.8369 ± 0.0385	0.6541 ± 0.0016
D_s^- Vertex quality & decay time	86.3516 ± 0.0857	0.4407 ± 0.0019	84.6257 ± 0.0662	0.5536 ± 0.0015
Number of tracks	100.0 ± 0	0.4407 ± 0.0019	99.9882 ± 0.0020	0.5535 ± 0.0015
D^0 veto	100.0 ± 0	0.4407 ± 0.0019	99.9941 ± 0.0014	0.5535 ± 0.0015
BDT	92.75563 ± 0.0684	0.4088 ± 0.0018	94.8596 ± 0.0429	0.5250 ± 0.0015
PID cuts, Λ_c^+ and D^+ veto, and D_s^- decay modes	23.70468 ± 0.0809	0.1045 ± 0.0006	51.1909 ± 0.1131	0.2688 ± 0.0010
Total		0.1045 ± 0.0006		0.2688 ± 0.0010

Table 3.3 – Summary of the relative and cumulative selection efficiencies for $\Lambda_b^0 \to D_s^- p$.

	Run 1		Run2	
	$\epsilon_{\text{rel}}(\%)$	$\epsilon_{\text{cum}}(\%)$	$\epsilon_{\text{rel}}(\%)$	$\epsilon_{\text{cum}}(\%)$
Generator level and Trigger	17.4608 ± 0.0041	17.4608 ± 0.0041	17.2135 ± 0.0042	17.2135 ± 0.0042
Reconstruction & Stripping	3.3405 ± 0.0050	0.5833 ± 0.0009	4.4501 ± 0.0059	0.7660 ± 0.0011
L0, HLT1, HLT2 cuts	96.0633 ± 0.0219	0.5603 ± 0.0009	95.5346 ± 0.0206	0.7318 ± 0.0010
Pion (transverse) momentum	95.0600 ± 0.0245	0.5326 ± 0.0009	94.6856 ± 0.0229	0.6929 ± 0.0010
Λ_c^+ mass window cuts	95.1588 ± 0.0249	0.5069 ± 0.0008	94.4979 ± 0.0239	0.6547 ± 0.0010
Λ_c^+ decay time	87.6323 ± 0.0399	0.4442 ± 0.0008	87.4851 ± 0.0363	0.5728 ± 0.0009
Number of tracks	99.9905 ± 0.0012	0.4441 ± 0.0008	99.9921 ± 0.0009	0.5727 ± 0.0009
BDT	99.5042 ± 0.0088	0.4419 ± 0.0008	94.4109 ± 0.0265	0.5407 ± 0.0009
PID Cuts	27.7334 ± 0.0012	0.1226 ± 0.0002	69.4491 ± 0.0584	0.3755 ± 0.0007
Total	0.1226 ± 0.0002		0.3755 ± 0.0007	

Table 3.4 – Summary of the relative and cumulative selection efficiencies for $\Lambda_b^0 \to \Lambda_c^+ \pi^-$.

Chapter 4

Fit Model

There are various components in the mass fits of $\Lambda_b^0 \to D_s^- p$ and $\Lambda_b^0 \to \Lambda_c^+ \pi^-$. The signal as well as background components are modelled using Monte Carlo samples. The modelling procedures of the signal and background components are described in Sections 4.1 and 4.2 respectively. The LHCb software package used to make the fit is B2DXFitters.

4.1 Background Components

Various background components play a role in both the $\Lambda_b^0 \to D_s^- p$ and $\Lambda_b^0 \to \Lambda_c^+ \pi^-$ fit. We can divide these components into three categories:

Misidentified backgrounds In misidentified backgrounds a specific daughter particle is misidentified. For example, in the decay $B_s^0 \to D_s^- \pi^+$ the pion can be misidentified as a proton so that it becomes the same final state as that of the $\Lambda_b^0 \to D_s^- p$ decay.

Partially reconstructed backgrounds In some cases, a parent particle can decay to an excited daughter particle. This daughter particle can emit a π^0 or a photon. These emitted particles are not reconstructed and therefore there is some missing energy, shifting the reconstructed invariant mass down.

Combinatorial background The combinatorial background is caused by a random combination of particles that are reconstructed as signal. For example, in the $\Lambda_b^0 \to D_s^- p$ fit this could be a D_s^- meson paired with a random proton from another process. Most of this background is removed by the BDT cut, but it is not completely eliminated.

The misidentified and partially reconstructed background are modelled using Monte Carlo simulation templates, whereas the combinatorial background is studied using the D_s^- sidebands of the data.

4.1.1 Modelling of Misidentified and Partially Reconstructed Background

The shapes of the misidentified and partially reconstructed backgrounds are obtained from Monte Carlo simulations. We apply the same kinematic cuts as for the corresponding data sample. Using the information obtained from `PIDCalib` (see Sec. 3.4.3) we are also able to correct for PID cuts. These shape is parametrised using density estimation (RooKeysPdf) [38] using the parameter ρ to ensure the smoothness of these templates. An example template is shown in Fig. 4.1, all other templates are shown in Appendix B. These templates are then used for the data fit in Sec. 5.1 and Sec. 5.2.

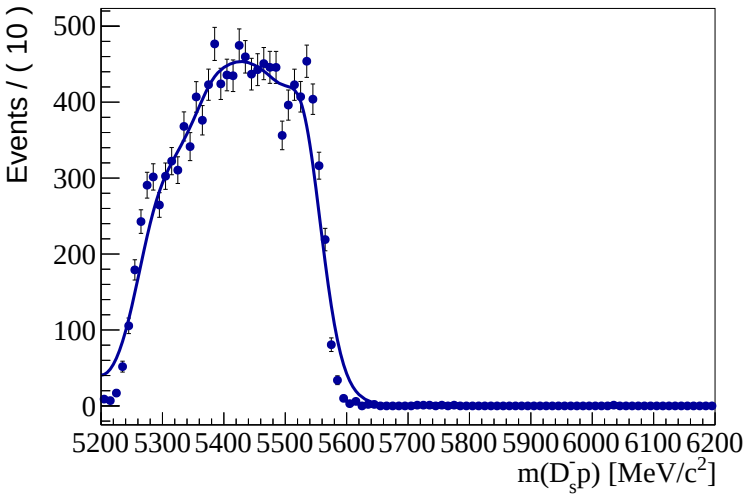

Figure 4.1 – The background template for $\Lambda_b^0 \to D_s^{*-} p$ for 2012, $\sqrt{s} = 8\text{TeV}$, simulation $p\ p$ sample. The slight discrepancy around the $m_{D_s^- p} \sim 5600\,\text{MeV}/c^2$ is to ensure the smoothness of the curve.

4.1.2 Modelling of Combinatorial Background

In order to find an appropriate shape for the combinatorial background, we plot the $\Lambda_b^0 \to D_s^- p$ data, except we select the sidebands of the D_s^- mass peak rather than the mass peak itself. In Fig 4.2 it is shown that the D_s^- mass peak is very clean. We look at the two cases, $m(K^-K^+\pi^-) < 1930\,\text{MeV}/c^2$ and $m(K^-K^+\pi^-) > 2010\,\text{MeV}/c^2$. The cut ensures we only have combinatorial background. The distributions of the combinatorial background are shown in Fig. 4.3. From these distributions we conclude that the combinatorial background can be modelled by an exponential function.

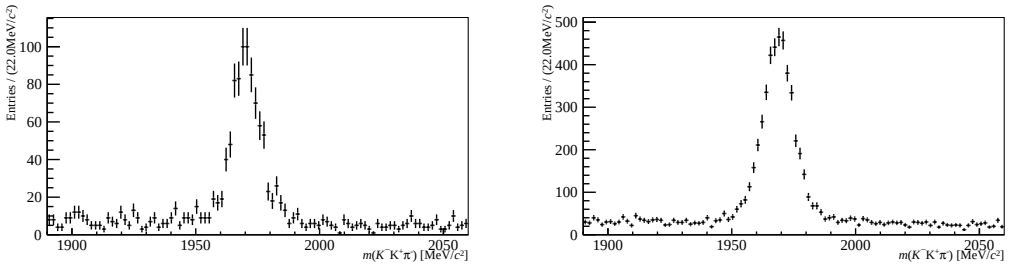

(a) Run 1 **(b)** Run 2

Figure 4.2 – The D_s^+ mass peak in the $K^-K^+\pi^-$ invariant mass for Run 1 and Run 2.

4.1.3 Peaking backgrounds

Potential backgrounds for the $\Lambda_b^0 \to D_s^- p$ decay can be a Λ_b^0 or B decays to four hadrons without an intermediate D_s^- meson. These backgrounds can be studied using the Λ_b^0 invariant mass spectrum while selecting the D_s^- candidate sidebands. The distributions, as shown in Fig 4.3, do not show any significant peaking structure and therefore we conclude that the decays from Λ_b^0 or B into four hadrons, without an intermediate D_s^- meson, are negligible.

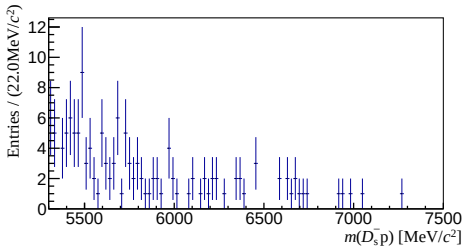

(a) Run 1, left D_s^- side band

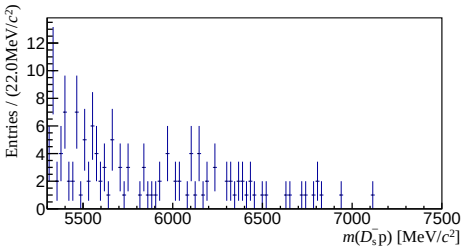

(b) Run 1, right D_s^- side band

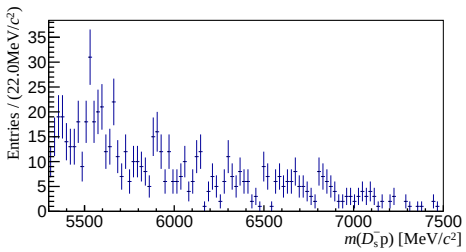

(c) Run 2, left D_s^- side band

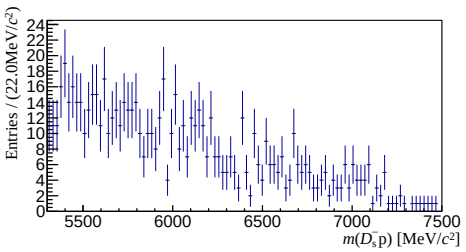

(d) Run 2, right D_s^- side band

Figure 4.3 – The distribution of the combinatorial background where we required $m(K^-K^+\pi^-) < 1930\,\text{MeV}/c^2$ for the left sideband and $m(K^-K^+\pi^-) > 2010\,\text{MeV}/c^2$ for the right sideband.

4.2 Signal Shape

4.2.1 Signal Shape for $\Lambda_b^0 \to D_s^- p$

The signal shape for the $\Lambda_b^0 \to D_s^- p$ candidates is described by a so-called double Crystal Ball [39], which is the sum of two Crystal Ball functions, $f_1 + f_2$, as given in Eqn (4.1), with a shared mean. This shape is formed out of a Gaussian shape, where one Gaussian tail transitions to an exponential tail. This shape ensures signal decays with a radiated photon or a poor resolution are correctly accounted for.

$$f_i(x;\overline{x},\alpha_i,n_i,\sigma_i) = N_i \cdot \begin{cases} \exp(-\frac{(x-\overline{x})^2}{2\sigma_i^2}), & \text{for } \frac{x-\overline{x}}{\sigma_i} > -\alpha_i \\ A_i \cdot (B_i - \frac{x-\overline{x}}{\sigma_i})^{-n_i}, & \text{for } \frac{x-\overline{x}}{\sigma_i} \leq -\alpha_i \end{cases} \tag{4.1}$$

$$\begin{aligned} A_i &= \left(\frac{n_i}{|\alpha_i|}\right)^n \cdot \exp\left(-\frac{|\alpha_i|^2}{2}\right) \\ B_i &= \frac{n_i}{|\alpha_i|} - |\alpha_i| \\ N_i &= \frac{1}{\sigma(C_i + D_i)} \\ C_i &= \frac{n_i}{|\alpha_i|} \cdot \frac{1}{n_i - 1} \cdot \exp\left(-\frac{|\alpha_i|^2}{2}\right) \\ D_i &= \sqrt{\frac{\pi}{2}}\left(1 + \text{erf}\left(\frac{|\alpha_i|}{\sqrt{2}}\right)\right) \end{aligned} \tag{4.2}$$

The function is described by four parameters: the Gaussian centre is described by the mean $\overline{x}$ and the standard deviation σ_i. The exponential tail is described by the exponents n_i. The point where the Gaussian centre transitions to the exponential tail is given by α_i (in units of σ_i). The constants A_i, B_i, C_i, D_i, N_i are given in

Eqn. (4.2). To form the sum of two Crystal Ball shapes, we choose that $\alpha_1 < 0$ and $\alpha_2 > 0$, such that we have two exponential tails on the opposite sides of the mean. We choose the fraction between these two Crystal Ball shapes to be $\text{Frac}_{\text{CBs}} = 0.5$, e.g. $\int f_1 dx / \int (f_1 + f_2) dx = 0.5$.

4.2.2 Signal Shape for $\Lambda_b^0 \to \Lambda_c^+ \pi^-$

The signal shape for the $\Lambda_b^0 \to \Lambda_c^+ \pi^-$ candidates is described by the sum of the so-called Ipatia and JohnsonSU functions with a shared mean. The Ipatia function has a hyperbolic core and is described by Eqn. (4.3), where $h(x; \overline{x}, \sigma, \lambda, \zeta, \beta)$ is described in Eqn. (4.4) and $h'(x; \overline{x}, \sigma, \lambda, \zeta, \beta)$ is its derivative with respect to x [40]. The function is described through several parameters, where $\overline{x}$ describes the mean of this function, and $K_{\lambda - \frac{1}{2}}$ are the special Bessel functions of third kind.

$$
\begin{aligned}
&H(x; \overline{x}, \sigma_I, \lambda, \zeta, \beta, a_1, n_1, a_2, n2) \propto \\
&\begin{cases}
h(x; \overline{x}, \sigma_I, \lambda, \zeta, \beta), & \text{if } \frac{x-\overline{x}}{\sigma_I} > -a_1 \text{ or } \frac{x-\overline{x}}{\sigma_I} < a_2, \\
\dfrac{h(x - a_1\sigma_I; \overline{x}, \sigma_I, \lambda, \zeta, \beta)}{\left(1 - m/\left(n \dfrac{h(x - a_1\sigma_I; \overline{x}, \sigma_I, \lambda, \zeta, \beta)}{h'(x - a_1\sigma_I; \overline{x}, \sigma_I, \lambda, \zeta, \beta)} - a_1\sigma_I\right)\right)^{n_1}}, & \text{if } \frac{x-\overline{x}}{\sigma_I} \leq -a_1 \\
\dfrac{h(x - a_2\sigma_I; \overline{x}, \sigma_I, \lambda, \zeta, \beta)}{\left(1 - m/\left(n \dfrac{h(x - a_2\sigma_I; \overline{x}, \sigma_I, \lambda, \zeta, \beta)}{h'(x - a_2\sigma_I; \overline{x}, \sigma_I, \lambda, \zeta, \beta)} - a_2\sigma_I\right)\right)^{n_2}}, & \text{if } \frac{x-\overline{x}}{\sigma_I} \geq a_2.
\end{cases}
\end{aligned}
\tag{4.3}
$$

$$
h(x; \overline{x}, \sigma_I, \lambda, \zeta, \beta) \propto ((x - \overline{x})^2 + A_\lambda^2(\zeta)\sigma_I^2)^{\frac{1}{2}\lambda - \frac{1}{4}} e^{\beta(x-\overline{x})} K_{\lambda-\frac{1}{2}} \left(\zeta \sqrt{1 + \left(\frac{x - \overline{x}}{A_\lambda(\zeta)\sigma_I} \right)^2} \right)
\tag{4.4}
$$

To the Ipatia function we add the JohnsonSU function. The key feature of the JohnsonSU function is its highly asymmetric tails. This function is described in Eqn. (4.5) [41], where $\overline{x}$ describes the mean, whereas the constants w, ω, c, z, and r are described in Eqn. (4.6). We name the sum of these two functions the IpatiaPlusJohnsonSU function and define its ratio by $\text{Frac}_{\text{I}} = \int I dx / \int (I + J) dx$.

$$
J(x; \overline{x}, \sigma_J, \nu, \tau) \propto \frac{1}{2\pi c(\nu, \tau)\sigma_J} e^{-\frac{1}{2} r(x, \overline{x}, \sigma_J, \nu, \tau)^2} \frac{1}{\tau \sqrt{z(x, \overline{x}, \sigma_J, \nu, \tau)^2 + 1}}
\tag{4.5}
$$

$$
\begin{aligned}
w &= e^{\tau^2} \\
\omega &= -\nu\tau \\
c &= \frac{1}{\sqrt{\frac{1}{2}(w-1)(w\cosh 2\omega + 1)}} \\
z &= \frac{m - (\overline{x} + c + \sigma_J \sqrt{w} \sinh \omega)}{c\sigma_J} \\
r &= -\nu + \frac{\sinh z^{-1}}{\tau}
\end{aligned}
\tag{4.6}
$$

Chapter 5

Signal Yield

To perform the fit of both decay channels, we combine the components described in Chapter 4 using the fit package called `B2DXFitters`. First we perform the fit of the $\Lambda_b^0 \to D_s^- p$ decay in Sec. 5.1, after which we perform the fit of the decay $\Lambda_b^0 \to \Lambda_c^+ \pi^-$ in Sec. 5.2.

5.1 Fit of $\Lambda_b^0 \to D_s^- p$ Signal

In order to find the signal shape parameters and to constrain these, we first perform a fit of the Double Crystal Ball function, as described in Sec. 4.2.1, to the simulation of the $\Lambda_b^0 \to D_s^- p$ decay for both runs. The results of these fits are shown in Fig. 5.1 and in Table 5.1. In the fit to the data, the mean ($\overline{x}$) is free to float. Both standard deviations (σ_1 and σ_2) are fixed in the fit, but they are both allowed to be scaled by the shared parameter R. All other variables are constrained to the values as shown in Table 5.1.
Using the found parameters for the signal shape, we perform the fit in the mass range $m_{D_s^- p} \in [5200, 6200]$, whose results are shown in Fig. 5.2 and in Table 5.2. The shift of the Λ_b^0 mass in the Run 1 fit is caused by the momentum calibration in this run. This fit yields 158 ± 11 $\Lambda_b^0 \to D_s^- p$ events for Run 1 and 335 ± 22 $\Lambda_b^0 \to D_s^- p$ events for Run 2. Combining these results gives a total yield of 493 ± 25 for $\Lambda_b^0 \to D_s^- p$.
To estimate the significance of this decay we study the chi-square with respect to the chi-square of the null-hypothesis. This yields a significance of 10.5σ for Run 1, a significance of 17.0σ for Run 2, which results in a combined significance of 20.0σ.

Parameter	Fit Value		Used in fit to data
	Run 1	Run 2	
Mean ($\overline{x}$)	5620.5 ± 0.2	5621.0 ± 0.13	
σ_1	16.32 ± 0.45	16.14 ± 0.49	✓
σ_2	11.92 ± 0.40	11.41 ± 0.36	✓
n_1	1.57 ± 0.46	2.53 ± 0.51	✓
n_2	1.23 ± 0.12	1.35 ± 0.10	✓
α_1	-2.50 ± 0.18	-2.02 ± 0.14	✓
α_2	2.11 ± 0.1	1.87 ± 0.08	✓
Frac_{CBs}	0.5	0.5	✓

Table 5.1 – Values from the fit of a Double Crystal Ball to the simulation of the decay $\Lambda_b^0 \to D_s^- p$. The variables with a marked check are fixed in the fit to the data.

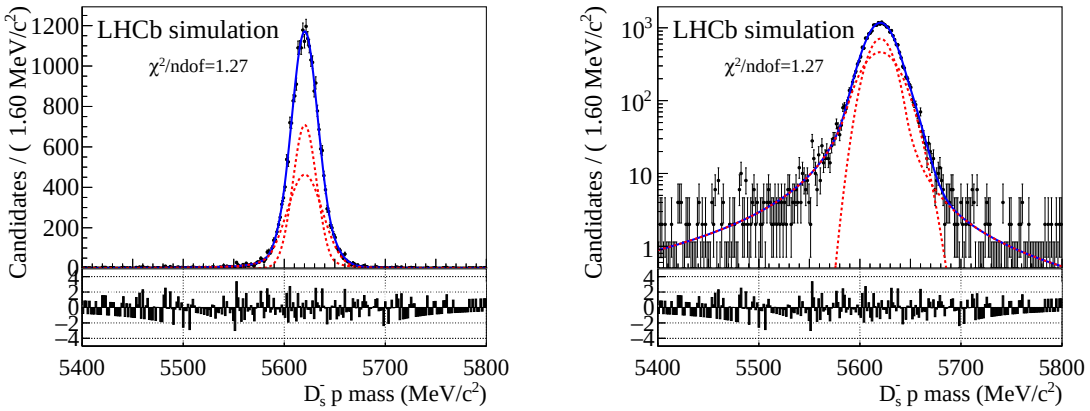

(a) Run 1

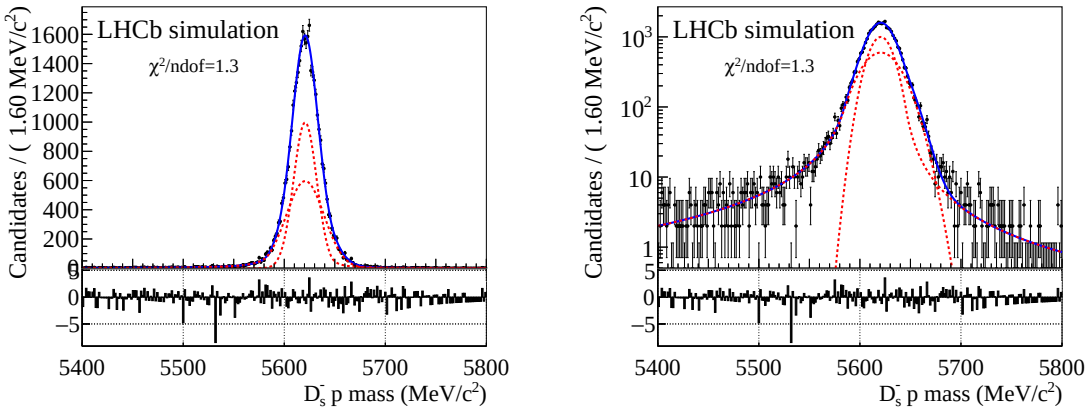

(b) Run 2

Figure 5.1 – Double Crystal Ball function fit for the simulation of $\Lambda_b^0 \to D_s^- p$. On the left, we see the linear scale, whereas on the right the fit is shown in logarithmic scale. The yellow and red parts are the two Crystal Balls as described in Eqn. (4.1). The blue line is the sum of these two components used to describe the peak.

Parameter	Fit Value	
	Run 1	Run 2
$N_{\Lambda_b^0 \to D_s^- p}$	158 ± 11	335 ± 22
$N_{B_s^0 \to D_s^{-(*)}(\pi^+,\rho)} + N_{B_s^0 \to D_s^{\mp(*)} K^{\pm(*)}}$	255 ± 25	428 ± 106
$N_{\Lambda_b^0 \to D_s^{*+} p}$	246 ± 21	339 ± 74
$N_{\text{combinatorial}}$	139 ± 19	243 ± 38
Mean	5629.0 ± 1.8	5621.5 ± 1.0
Combinatorial Exponent	-0.00125 ± 0.00037	-0.00000 ± 0.00032
R	1.208 ± 0.086	1.096 ± 0.055

Table 5.2 – Fit results from the data of the decay $\Lambda_b^0 \to D_s^- p$.

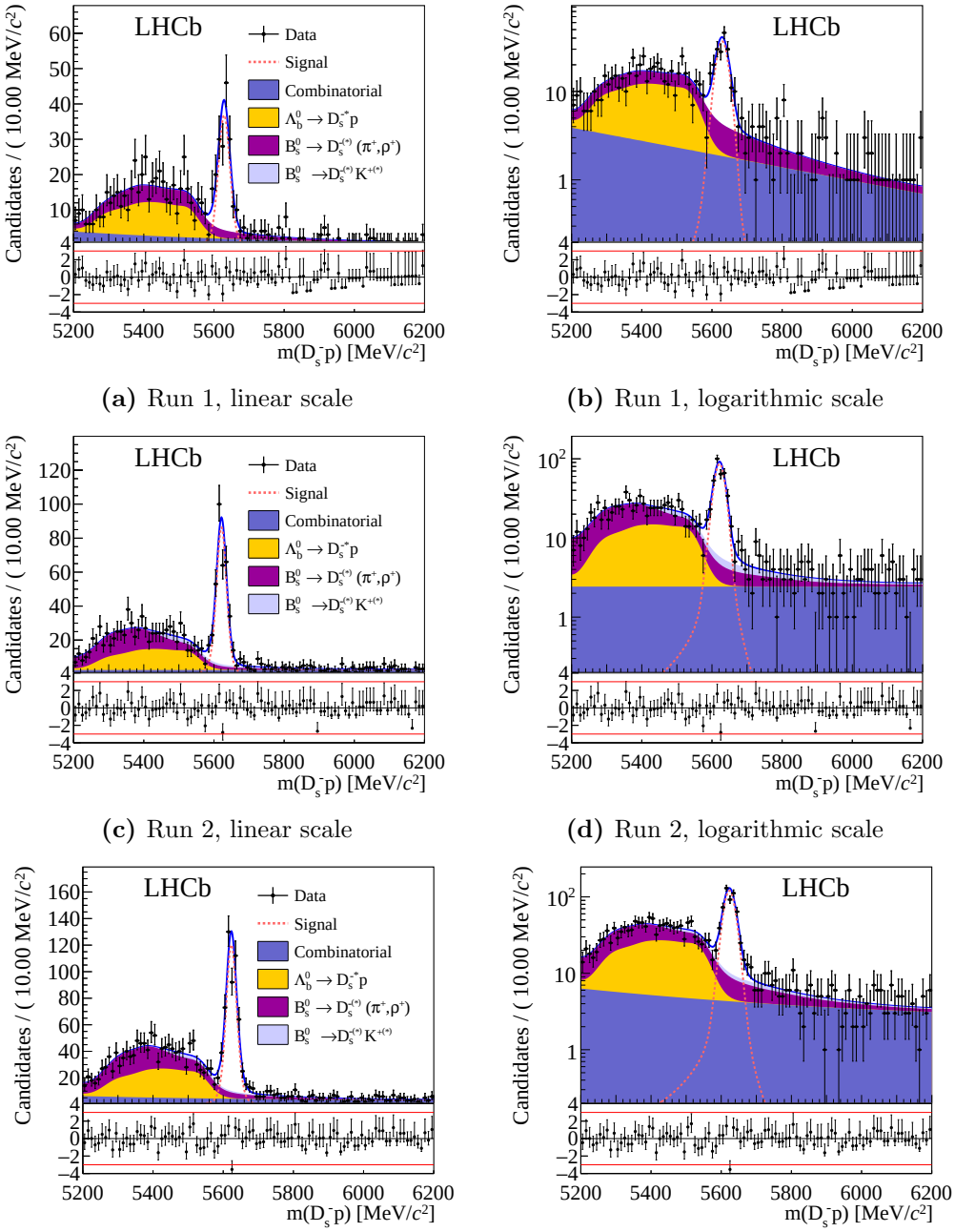

(a) Run 1, linear scale

(b) Run 1, logarithmic scale

(c) Run 2, linear scale

(d) Run 2, logarithmic scale

(e) Both runs, linear scale

(f) Both runs, logarithmic scale

Figure 5.2 – The mass fit of the decay $\Lambda_b^0 \to D_s^- p$ for both runs separate and summed, in linear and logarithmic scale.

5.2 Fit of $\Lambda_b^0 \to \Lambda_c^+ \pi^-$ Signal

In order to extract a value for the branching fraction of the decay $\Lambda_b^0 \to D_s^- p$, the signal yield is normalised with respect to the normalisation channel $\Lambda_b^0 \to \Lambda_c^+ \pi^-$ with the known branching fraction of $(4.9 \pm 0.4)\%$ [5]. To find the signal shape parameters and to constrain these, we first perform a fit of the the IpatiaPlusJohnsonSU function, as described in Sec. 4.2.2, to the simulation of the $\Lambda_b^0 \to \Lambda_c^+ \pi^-$ decay for both runs. The results of these fits are shown in Fig. 5.3 and in Table 5.3. In the fit to the data, the mean ($\overline{x}$), ν, τ, and both standard deviations (σ_I and σ_J) are left free to float, all other variables are constrained to the values as shown in Table 5.3.
Using the parameters as found in the simulation for the signal shape, we perform the fit in the mass range $m_{\Lambda_c^+ \pi^-} \in [5400, 6200]$, where the results are shown in Fig. 5.4 and in Table 5.4. The higher than expected mean for Run 1 is caused by the momentum calibration of this run. This fit yields 103257 ± 341 $\Lambda_b^0 \to \Lambda_c^+ \pi^-$ events for Run 1 and 221194 ± 586 $\Lambda_b^0 \to \Lambda_c^+ \pi^-$ events for Run 2. Combining these results gives a total yield of 324451 ± 678 for $\Lambda_b^0 \to \Lambda_c^+ \pi^-$.

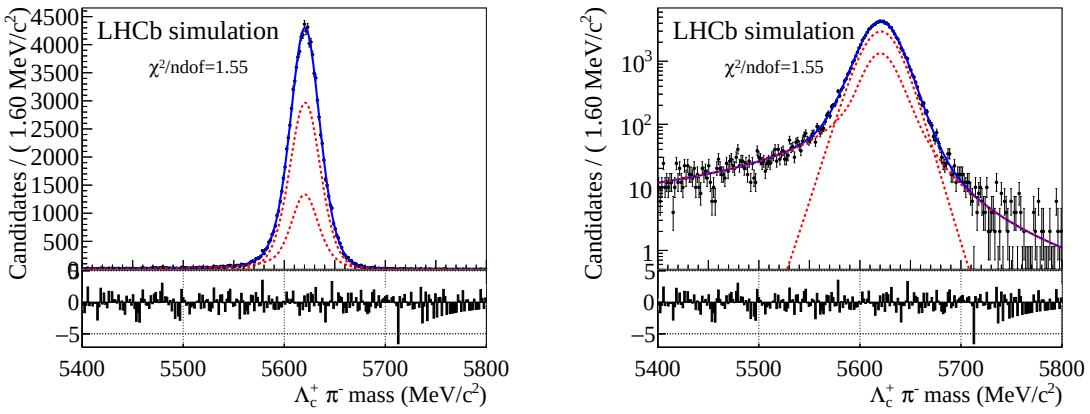

(a) Run 1

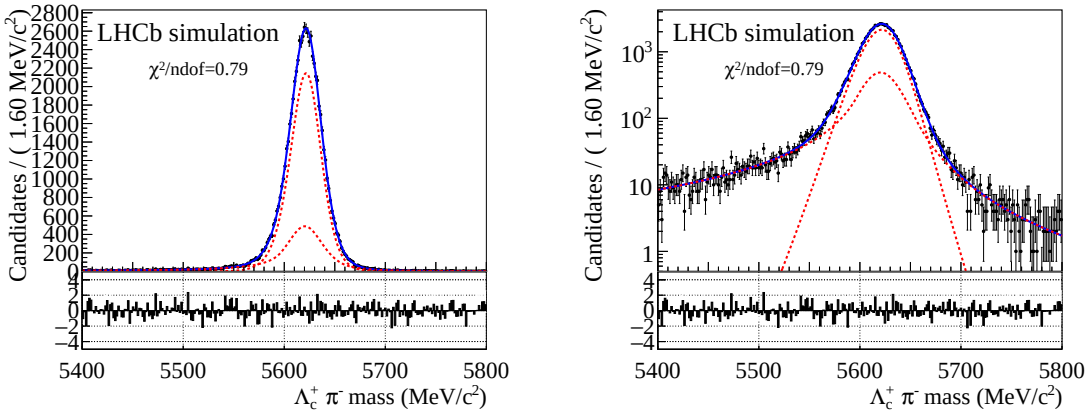

(b) Run 2

Figure 5.3 – IpatiaPlusJohnsonSU function fit for the simulation of $\Lambda_b^0 \to \Lambda_c^+ \pi^-$. On the left we see the linear scale, whereas on the right the fit is shown in logarithmic scale. The two red dashed functions are the Ipatia and JohnsonSU functions as described in Eqn. (4.3) and Eqn. (4.5). The blue line is the sum of these two components used to describe the peak.

Parameter	Fit Value		Used in fit to data
	Run 1	Run 2	
Mean ($\overline{x}$)	5620.284 ± 0.092	5620.41 ± 0.14	
σ_I	19.8 ± 4.4	25.3 ± 4.1	
σ_J	17.19 ± 0.58	17.37 ± 0.35	
a_1	1.29 ± 0.39	0.93 ± 0.32	✓
a_2	1.86 ± 0.30	1.40 ± 0.31	✓
Frac_I	0.32 ± 0.12	0.248 ± 0.096	✓
n_1	1.199 ± 0.095	1.41 ± 0.22	✓
n_2	2.72 ± 0.46	2.48 ± 0.39	✓
ν	-0.128 ± 0.080	-0.330 ± 0.093	
τ	0.384 ± 0.063	0.423 ± 0.026	
λ	-2.11 ± 0.75	-2.11	✓
ζ	0.0	0.0	✓
β	0.0	0.0	✓

Table 5.3 – Values from the fit of an IpatiaPlusJohnsonSU function to the simulation of the decay $\Lambda_b^0 \to \Lambda_c^+ \pi^-$. The variables with a marked check are fixed in the fit to the data.

Parameter	Fit Value	
	Run 1	Run 2
$N_{\Lambda_b^0 \to \Lambda_c^+ \pi^-}$	103257 ± 341	221194 ± 586
$N_{B^0 \to D^- \pi^+}$	4861 ± 260	20051 ± 661
$N_{B_s^0 \to D_s^- \pi^+}$	0 ± 33	0 ± 1004
$N_{\text{combinatorial}}$	1598 ± 95	50464 ± 1377
$N_{\Lambda_b^0 \to \Lambda_c^+ K^-}$	587 ± 587	5703 ± 520
$N_{\Lambda_b^0 \to \Lambda_c^+ \rho}$	3133 ± 307	31221 ± 3802
$N_{\Lambda_b^0 \to \Sigma_c \pi^-}$	21097 ± 306	21007 ± 3017
Mean ($\overline{x}$)	5623.806 ± 0.073	5619.785 ± 0.074
Combinatorial Exponent	-0.00000 ± 0.00011	-0.003924 ± 0.000098
σ_I	20.51 ± 0.41	24.35 ± 0.71
σ_J	18.75 ± 0.13	18.21 ± 0.10
ν	-0.256 ± 0.011	-0.058 ± 0.048
τ	0.289 ± 0.021	0.335 ± 0.012

Table 5.4 – Fit results to data from the decay $\Lambda_b^0 \to \Lambda_c^+ \pi^-$.

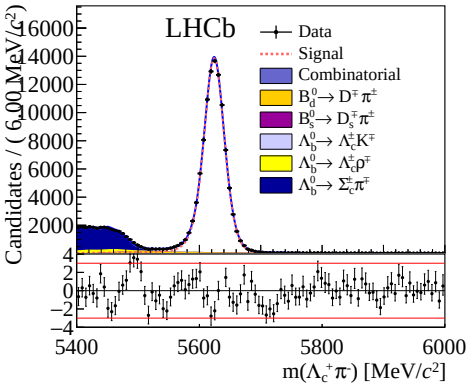

(a) Run 1, linear scale

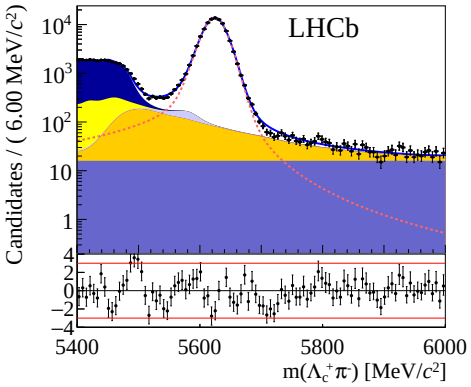

(b) Run 1, logarithmic scale

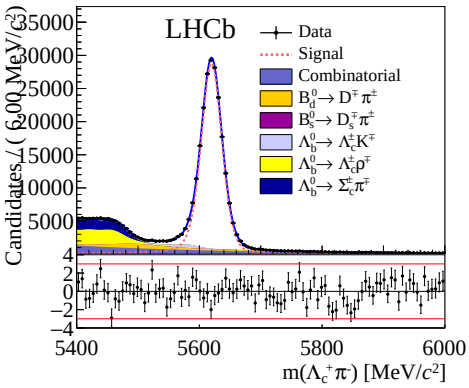

(c) Run 2, linear scale

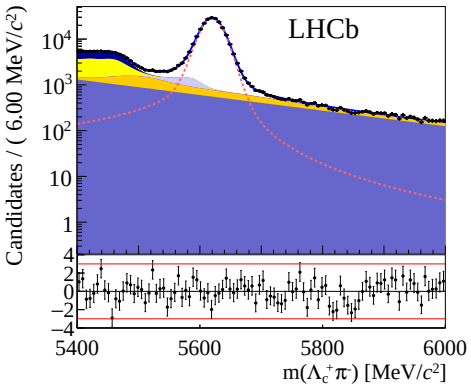

(d) Run 2, logarithmic scale

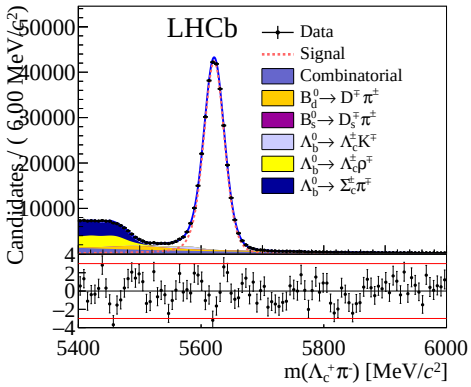

(e) Both runs, linear scale

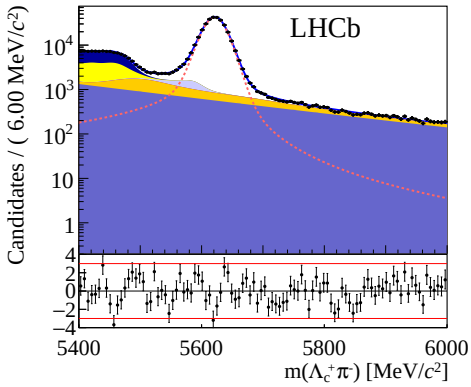

(f) Both runs, logarithmic scale

Figure 5.4 – The mass fit of the decay $\Lambda_b^0 \to \Lambda_c^+ \pi^-$ for both runs separate and summed, in linear and logarithmic scale.

Chapter 6

Systematic Uncertainties

In order to obtain a full overview of the uncertainties, it is also important to study the systematic uncertainties. An overview of the systematic uncertainties to be studied is listed below.

PID efficiencies The systematic uncertainty of the PID cuts is especially important to study, since there is only little reference data available for the proton efficiencies. Therefore, it is likely that this component of the systematic uncertainties will dominate the uncertainty on the branching fraction of $\Lambda_b^0 \to D_s^- p$. One can study the behaviour of the efficiency when different bins are chosen in `PIDCalib` to compute the efficiency in that particular bin. To decrease the systematic uncertainty on this component, it might be possible to choose protons from the $\Lambda_b^0 \to \Lambda_c^+ \pi^-$ sample in the same momentum range and with the same number of tracks as those of the $\Lambda_b^0 \to D_s^- p$ sample. Using this, the uncertainties can largely cancel in the branching fraction calculation.

Signal shape One can study different signal shapes for the signal peaks. For the $\Lambda_b^0 \to D_s^- p$ fit one can implement an Ipatia or Johnson function, or its sum IpatiaPlusJohnsonSU, as defined in Sec 4.2.2, to see how that will affect the signal yield. For the $\Lambda_b^0 \to \Lambda_c^+ \pi^-$ one can leave more free parameters in the final fit, to study how that affects the signal yield.

Efficiency on L0 trigger The L0 trigger has an asymmetry in the detection efficiency between pions and kaons, which is dependent on the transverse momentum p_{T} [42]. This difference is not implemented in the simulation and therefore, needs be to taken into account.

Exclusion of small backgrounds Currently, there are some ignored backgrounds in the $\Lambda_b^0 \to \Lambda_c^+ \pi^-$ fit. The potential backgrounds for this fit are $B^0 \to D^+ \rho^-$ and $B^0 \to D_s^+ \pi^-$. One could include these backgrounds in the fit to see its behaviour and the signal yield including these backgrounds.

BDT efficiency The BDT cut to reduce the combinatorial background is mostly based on kinematic variables that are well modelled in simulation. However, the BDT cut is also dependent on the track chisquare, which is less well modelled in simulation. This effect needs to be studied and taken into account.

Smoothness of templates In order to make the background templates, one has to set certain smoothness to the templates. Adjusting the parameter ρ that describes the smoothness of the templates can result in a different signal yield. Therefore, this needs to be taken into account.

Combinatorial shape In both fits, we chose an exponential function to describe the combinatorial background. In order to check the influence of this choice, we can also describe the combinatorial background as an exponential function with an offset, or a double exponential function, in order to study the effects of this choice.

Chapter 7

Results

In this chapter we first discuss the branching ratio of the decay $\Lambda_b^0 \to D_s^- p$ in Sec. 7.1. In Sec. 7.2 we discuss the measurement of $|V_{ub}|\,|a_{NF}|$.

7.1 Branching Fraction

The yields and efficiencies of the $\Lambda_b^0 \to D_s^- p$ and $\Lambda_b^0 \to \Lambda_c^+ \pi^-$ decays are summarised in Table 7.1 as obtained in Sec. 3.5, 5.1, and 5.2.

Parameter	Fitted Value	
	Run 1	Run 2
$N_{\Lambda_b^0 \to D_s^- p}$	158 ± 11	335 ± 22
$\epsilon_{\Lambda_b^0 \to D_s^- p}$	0.1045 ± 0.0006	0.2688 ± 0.0010
$N_{\Lambda_b^0 \to \Lambda_c^+ \pi^-}$	103257 ± 341	221194 ± 586
$\epsilon_{\Lambda_b^0 \to \Lambda_c^+ \pi^-}$	0.1126 ± 0.0002	0.3755 ± 0.0007

Table 7.1 – Summary of the obtained yields and efficiencies.

We use the following equation to calculate the branching fraction of $\Lambda_b^0 \to D_s^- p$:

$$B(\Lambda_b^0 \to D_s^- p) = B(\Lambda_b^0 \to \Lambda_c^+ \pi^-) \times \frac{N(\Lambda_b^0 \to (D_s^- \to K^- K^+ \pi^-) p)}{N(\Lambda_b^0 \to (\Lambda_c^+ \to p K^- \pi^+) \pi^-)} \times \frac{\epsilon(\Lambda_b^0 \to (\Lambda_c^+ \to p K^- \pi^+) \pi^-)}{\epsilon(\Lambda_b^0 \to (D_s^- \to K^- K^+ \pi^-) p)} \times \frac{B(\Lambda_c^+ \to p K^- \pi^+)}{B(D_s^- \to K^- K^+ \pi^-)}, \quad (7.1)$$

as stated in Ch. 1. For the computation of the branching fraction we use the following values of branching fractions [5]:

$$B(\Lambda_b^0 \to \Lambda_c^+ \pi^-) = (4.9 \pm 0.4) \times 10^{-5}, \quad (7.2)$$

$$B(\Lambda_c^+ \to p K^- \pi^+) = (6.35 \pm 0.33) \times 10^{-2}, \quad (7.3)$$

$$B(D_s^- \to K^- K^+ \pi^-) = (5.45 \pm 0.17) \times 10^{-2}. \quad (7.4)$$

Using Eqn. (7.1) we compute the branching fraction for $\Lambda_b^0 \to D_s^- p$ to be:

$$\text{Run 1:} \quad B(\Lambda_b^0 \to D_s^- p) = (9.4 \pm 0.7(\text{stat.}) \pm 1.0(B)) \times 10^{-6}, \quad (7.5)$$

$$\text{Run 2:} \quad B(\Lambda_b^0 \to D_s^- p) = (12.1 \pm 0.8(\text{stat.}) \pm 1.2(B)) \times 10^{-6}, \quad (7.6)$$

$$\text{Combined:} \quad B(\Lambda_b^0 \to D_s^- p) = (10.7 \pm 0.5(\text{stat.}) \pm 1.1(B)) \times 10^{-6}, \quad (7.7)$$

where the first error is the statistical error, the second error is caused by the errors on the external branching fractions. We conclude that the results from Run 1 and Run 2 are consistent within 2.6σ, only taking the statistical errors into account, the systematic uncertainties are not taken into account yet. We also conclude that they are consistent with the current upper limit of $B(\Lambda_b^0 \to D_s^- p) < 4.8 \times 10^{-4}$.

7.2 $|V_{ub}|\,|a_{NF}|$

The branching ratio of $\Lambda_b^0 \to D_s^- p$ is directly related to the CKM-element $|V_{ub}|$ and the non-factorisable effect $|a_{NF}|$ as stated in Ch. 1. The relation between these parameters is given by [43–45]:

$$B(\Lambda_b^0 \to D_s^- p) = 6\pi^2 \tau_{\Lambda_b^0} |V_{cs}|^2 f_{D_s^-} |a_{NF}|^2 X_{D_s^-} F^2_{\Lambda_b^0 \to p}(m_{D_s^-}), \tag{7.8}$$

$$B(\Lambda_b^0 \to D_s^- p) = 6\pi^2 \tau_{\Lambda_b^0} |V_{cs}|^2 f_{D_s^-} |a_{NF}|^2 X_{D_s^-} \frac{\mathrm{d}\Gamma/dq^2}{|V_{ub}|^2}, \tag{7.9}$$

where $\tau_{\Lambda_b^0}$ is the lifetime of the Λ_b^0 baryon, $f_{D_s^-}$ is the decay constant of the D_s^- meson, $X_{D_s^-}$ is a scaling factor between the hadronic and semi-leptonic decays of the Λ_b^0 baryon to p and $F^2_{\Lambda_b^0 \to p}(m_{D_s^-})$ is the form factor of the decay Λ_b^0 to p. The form factor can also be expressed as the differential decay rate divided by the CKM-element V_{ub} $\dfrac{\mathrm{d}\Gamma/dq^2}{|V_{ub}|^2}$ as shown in Eqn. (7.9). This factor is theoretically predicted in Ref. [46] to be $(0.5 \pm 0.4) \times |V_{ub}|$, as shown in Fig. 7.1. Furthermore, there are accurate methods to determine $X_{D_s^-}$ for decaying B-mesons. However, there is not enough research done to compute this factor for the Λ_b^0-baryon decays [45]. Therefore, more study is needed for the determination of the factor $|V_{ub}|\,|a_{NF}|$ for this decay.

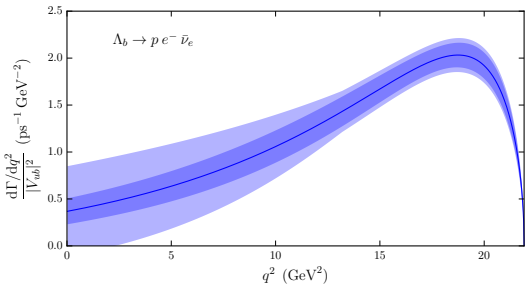

Figure 7.1 – Predictions for the $\Lambda_b^0 \to p e \overline{\nu}_e$ differential decay rates in the Standard Model, dependent of the invariant mass of the particle formed by the W-boson. The inner bands show the statistical uncertainty and the outer bands show the total uncertainty. Figure taken from Ref. [46].

Chapter 8

Conclusion and Outlook

The yields of the decays $\Lambda_b^0 \to D_s^- p$ and $\Lambda_b^0 \to \Lambda_c^+ \pi^-$ are determined using LHCb data from 2011, 2012, 2015, and 2016, corresponding to a total integrated luminosity of 4.9 fb. The signal significance of the decay $\Lambda_b^0 \to D_s^- p$ over the null-hypothesis is 20σ, resulting in the first observation of this decay.

The efficiencies of both decays were determined using Monte Carlo simulation and PID performance histograms. From this, the branching fraction of $B(\Lambda_b^0 \to D_s^- p) = (10.7 \pm 0.5(\text{stat.}) \pm 1.1(B)) \times 10^{-6}$ was calculated where the first error is statistical error and the second error from errors of external branching fractions.

8.1 Future Research

The next step in this analysis would to be perform a full study of the systematic uncertainties. The systematic uncertainty of the PID cuts is especially important to study, since there is only little data for the proton efficiencies. Therefore, it is likely that this component of the systematic uncertainties will dominate the uncertainty on the yield and branching fraction of $\Lambda_b^0 \to D_s^- p$.

Furthermore, it is important to perform the fit with the official LHCb simulation, where we used the `RapidSim` simulation due to the lack of official simulation at the time of writing, as described in Sec. 2.2. It is also important that these simulations are used to update the efficiencies of the $\Lambda_b^0 \to D_s^- p$ Run 2 sample in Table 3.3.

Additionally, it is important to further study the fits made for $\Lambda_b^0 \to D_s^- p$ and $\Lambda_b^0 \to \Lambda_c^+ \pi^-$. Background yields can be Gaussian constrained with respect to each other, in order to avoid backgrounds compensating for one another. Moreover, it is important to further study the Run 1 fit of $\Lambda_b^0 \to \Lambda_c^+ \pi^-$, to minimise the patterns in the pulls. A possible solution for this is to decrease the ProbNN_p cut for the proton coming from the Λ_c^+, in order to increase the statistics for this plot.

To expand this study, it would also be very interesting to further investigate the form factor of the Λ_b^0 to p transition ($F^2(\Lambda_b^0 \to p)$), the non-factorisable effect $|a_{NF}|$, and the scaling factor $X_{D_s^+}$ to obtain a measurement for the CKM-matrix $|V_{ub}|$.

Appendix A

Background fits

A.1 Run 1

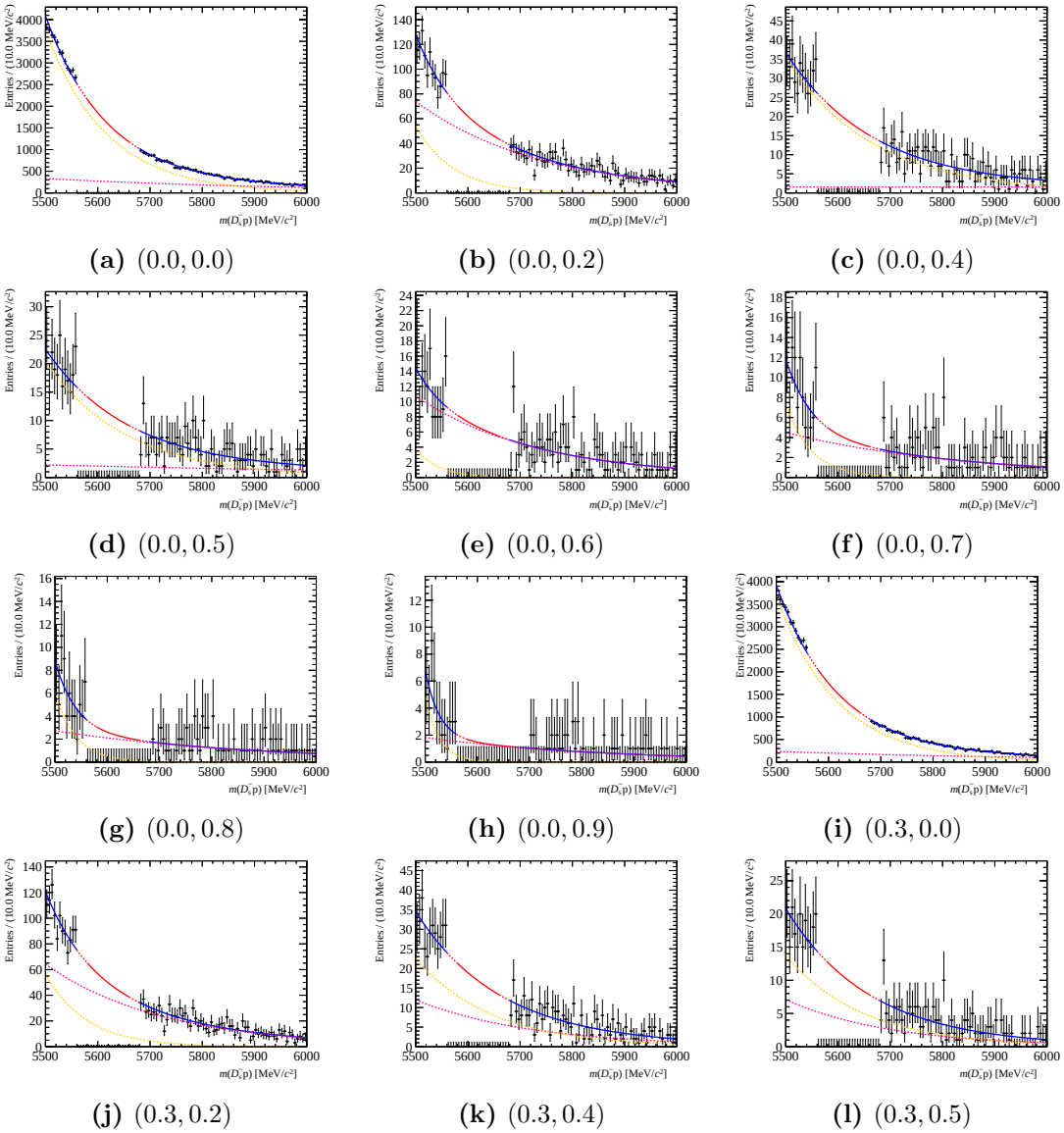

(a) $(0.0, 0.0)$ **(b)** $(0.0, 0.2)$ **(c)** $(0.0, 0.4)$

(d) $(0.0, 0.5)$ **(e)** $(0.0, 0.6)$ **(f)** $(0.0, 0.7)$

(g) $(0.0, 0.8)$ **(h)** $(0.0, 0.9)$ **(i)** $(0.3, 0.0)$

(j) $(0.3, 0.2)$ **(k)** $(0.3, 0.4)$ **(l)** $(0.3, 0.5)$

Figure A.1 – First part of Fig. A.1.

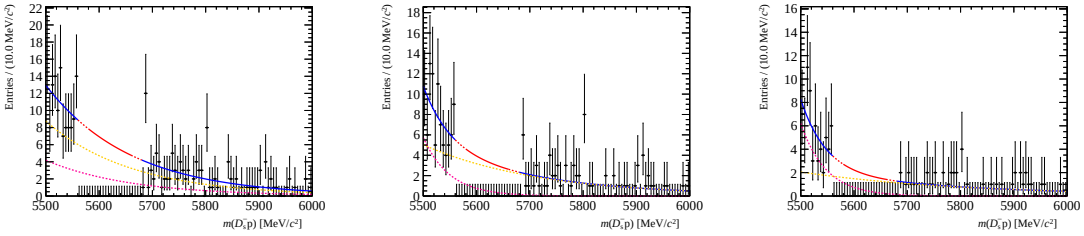

(m) $(0.3, 0.6)$ **(n)** $(0.3, 0.7)$ **(o)** $(0.3, 0.8)$

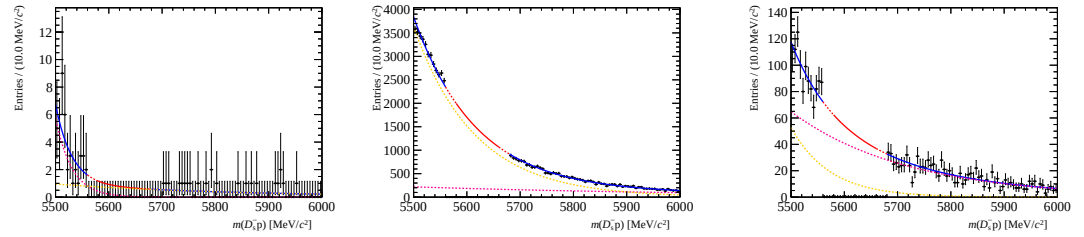

(p) $(0.3, 0.9)$ **(q)** $(0.4, 0.0)$ **(r)** $(0.4, 0.2)$

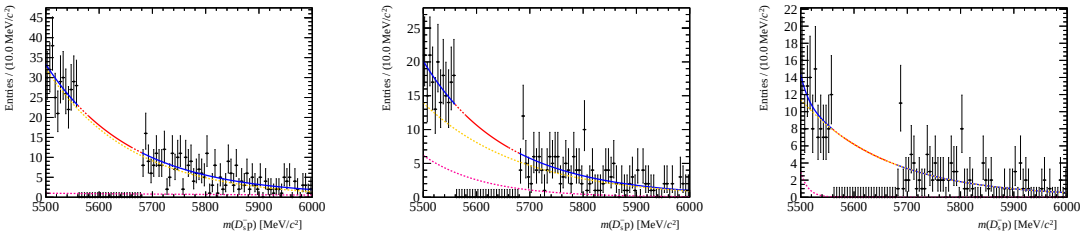

(s) $(0.4, 0.4)$ **(t)** $(0.4, 0.5)$ **(u)** $(0.4, 0.6)$

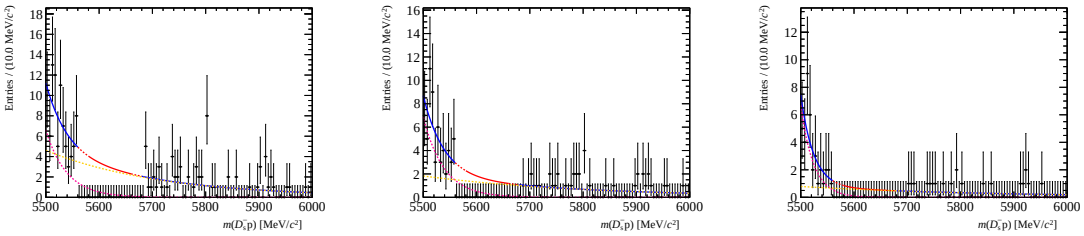

(v) $(0.4, 0.7)$ **(w)** $(0.4, 0.8)$ **(x)** $(0.4, 0.9)$

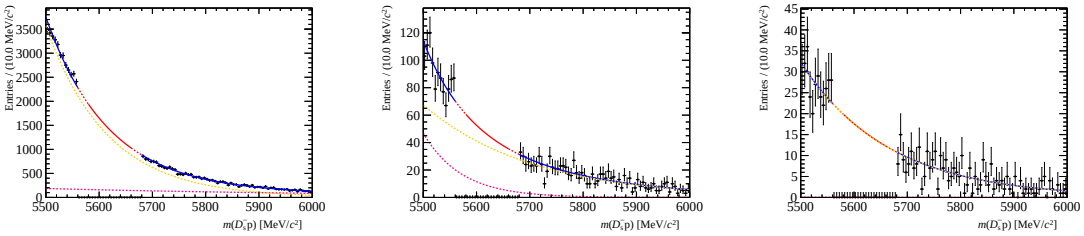

(y) $(0.5, 0.0)$ **(z)** $(0.5, 0.2)$ **(aa)** $(0.5, 0.4)$

Figure A.1 – Second part of Fig. A.1.

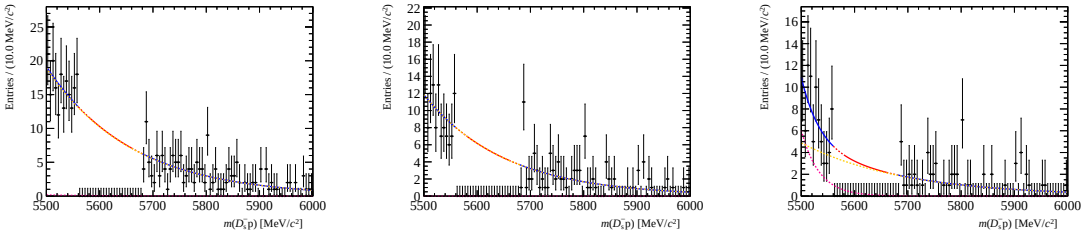

(ab) $(0.5, 0.5)$ **(ac)** $(0.5, 0.6)$ **(ad)** $(0.5, 0.7)$

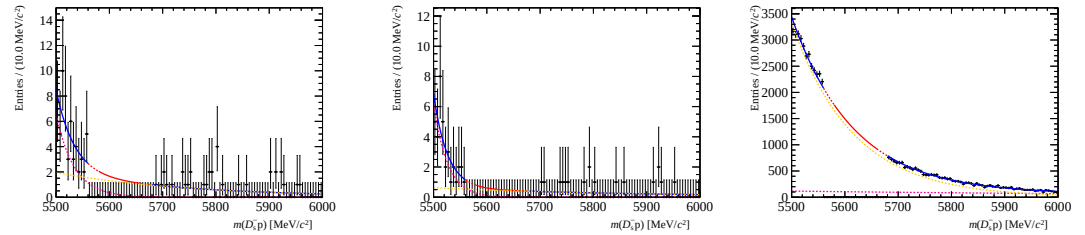

(ae) $(0.5, 0.8)$ **(af)** $(0.5, 0.9)$ **(ag)** $(0.7, 0.0)$

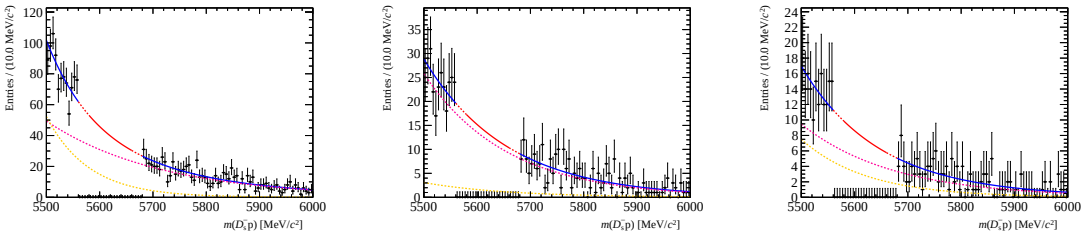

(ah) $(0.7, 0.2)$ **(ai)** $(0.7, 0.4)$ **(aj)** $(0.7, 0.5)$

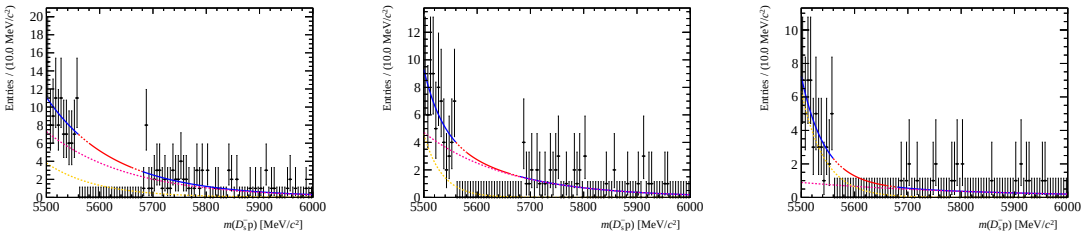

(ak) $(0.7, 0.6)$ **(al)** $(0.7, 0.7)$ **(am)** $(0.7, 0.8)$

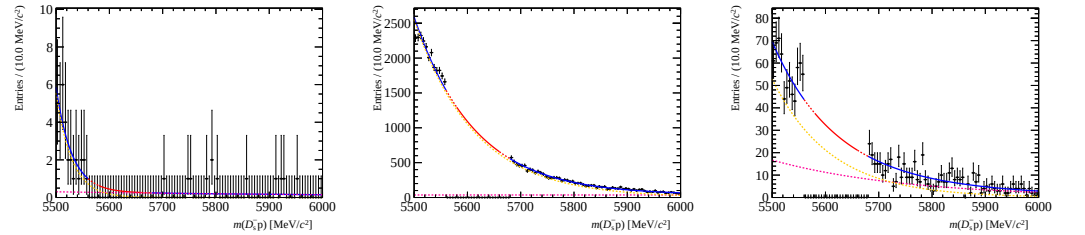

(an) $(0.7, 0.9)$ **(ao)** $(0.9, 0.0)$ **(ap)** $(0.9, 0.2)$

Figure A.1 – Third part of Fig. A.1.

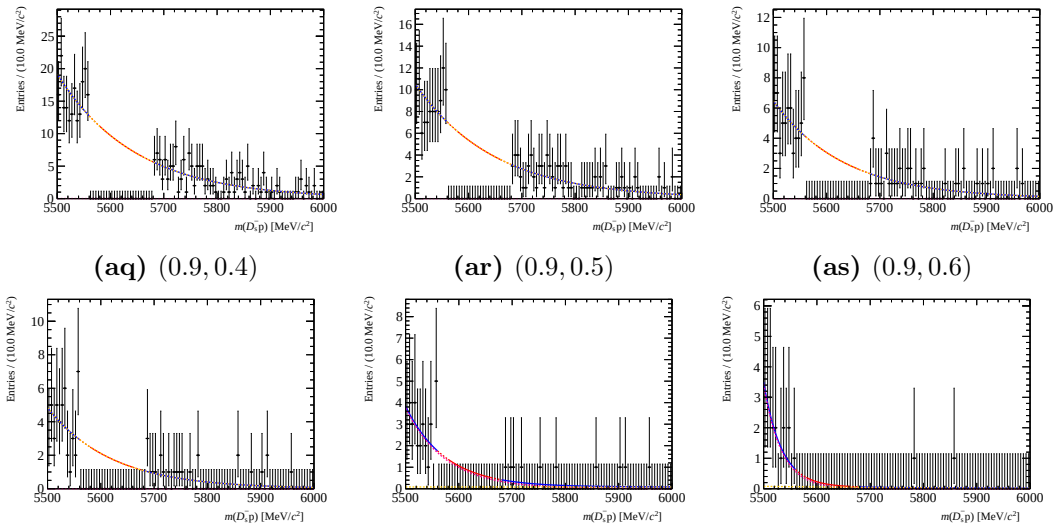

(aq) $(0.9, 0.4)$ **(ar)** $(0.9, 0.5)$ **(as)** $(0.9, 0.6)$

(at) $(0.9, 0.7)$ **(au)** $(0.9, 0.8)$ **(av)** $(0.9, 0.9)$

Figure A.1 – An extended selection of the fits used to estimate the background yield under the signal peak as described in Sec. 3.4.4 for Run 1. The cuts BDT $> \alpha$ and ProbNN$_p > \beta$ for each figure are displayed as (α, β). In these graphs, the pink and yellow dashed lines are the two exponential functions that describe the background. The blue and red parts are the sum of these two exponential functions. The fit is produced using only the data points that lie in the range of the blue line. The red solid line is used to compute the background events under the signal peak. The red dashed line is ignored in both the fit and the computation of the background events.

A.2 Run 2

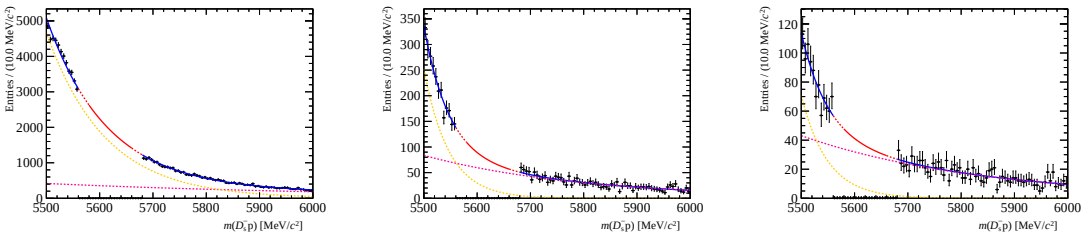

(a) $(0.0, 0.0)$ **(b)** $(0.0, 0.2)$ **(c)** $(0.0, 0.4)$

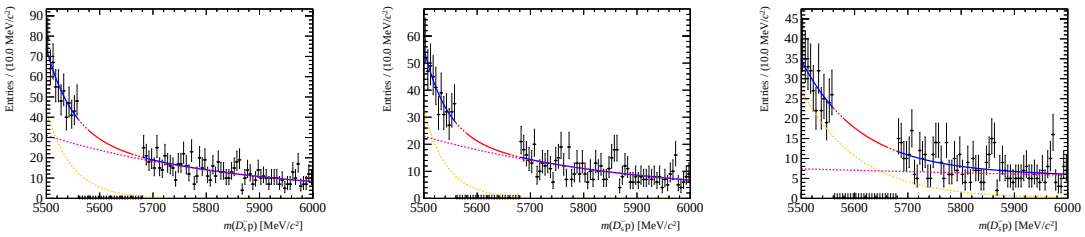

(d) $(0.0, 0.5)$ **(e)** $(0.0, 0.6)$ **(f)** $(0.0, 0.7)$

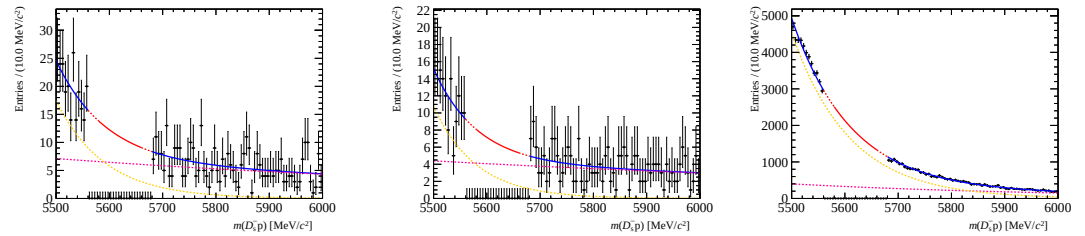

(g) $(0.0, 0.8)$ **(h)** $(0.0, 0.9)$ **(i)** $(0.3, 0.0)$

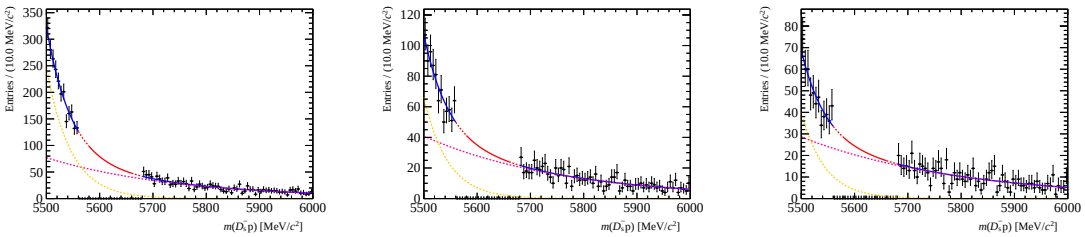

(j) $(0.3, 0.2)$ **(k)** $(0.3, 0.4)$ **(l)** $(0.3, 0.5)$

Figure A.2 – First part of Fig. A.2.

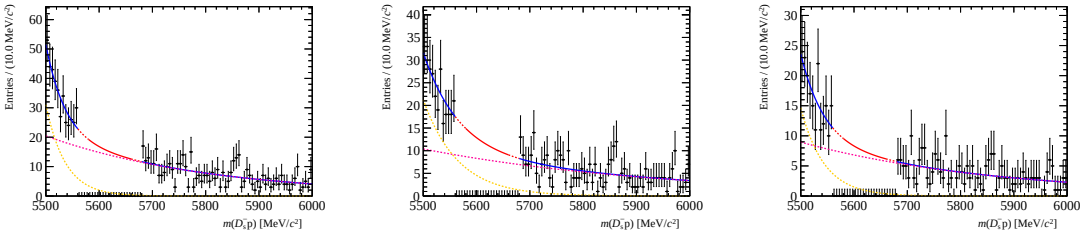

(m) $(0.3, 0.6)$ **(n)** $(0.3, 0.7)$ **(o)** $(0.3, 0.8)$

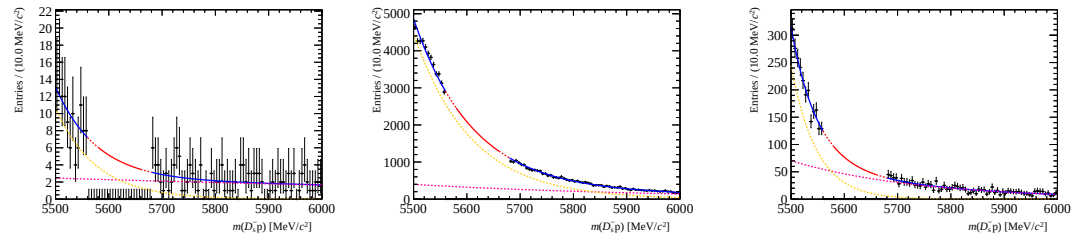

(p) $(0.3, 0.9)$ **(q)** $(0.4, 0.0)$ **(r)** $(0.4, 0.2)$

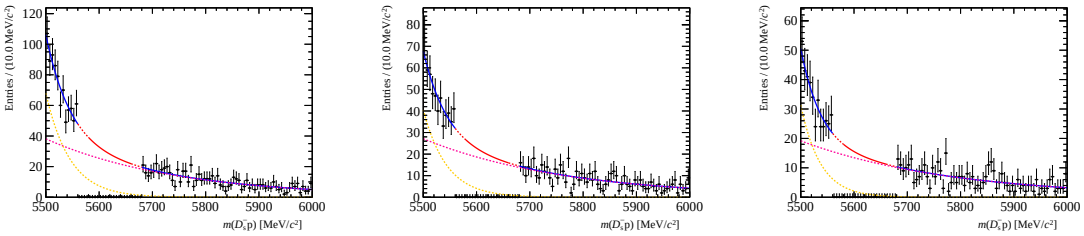

(s) $(0.4, 0.4)$ **(t)** $(0.4, 0.5)$ **(u)** $(0.4, 0.6)$

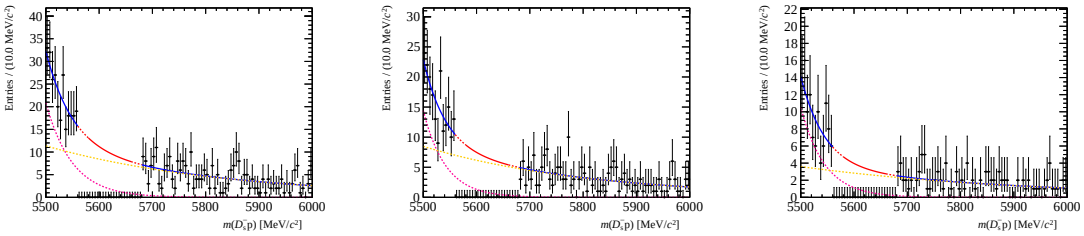

(v) $(0.4, 0.7)$ **(w)** $(0.4, 0.8)$ **(x)** $(0.4, 0.9)$

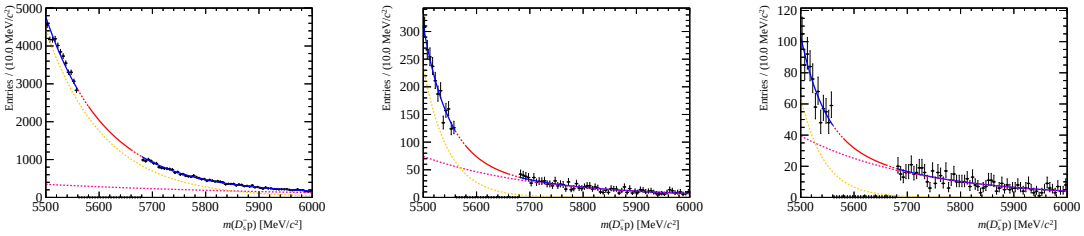

(y) $(0.5, 0.0)$ **(z)** $(0.5, 0.2)$ **(aa)** $(0.5, 0.4)$

Figure A.2 – Second part of Fig. A.2.

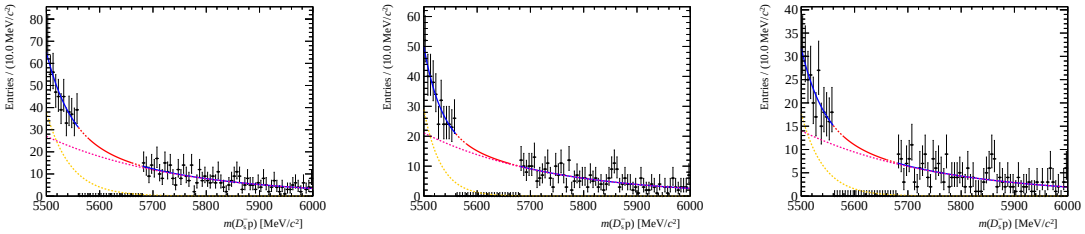

(ab) $(0.5, 0.5)$ **(ac)** $(0.5, 0.6)$ **(ad)** $(0.5, 0.7)$

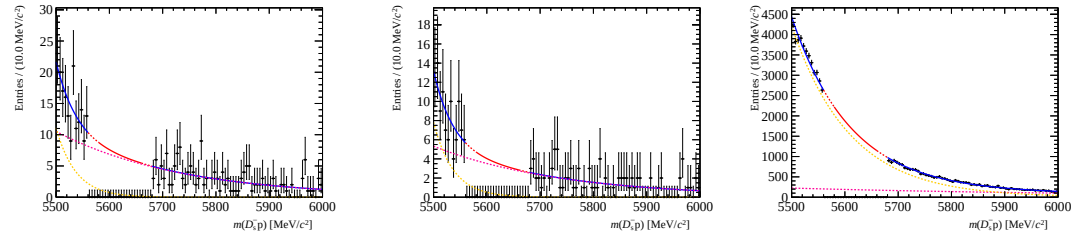

(ae) $(0.5, 0.8)$ **(af)** $(0.5, 0.9)$ **(ag)** $(0.7, 0.0)$

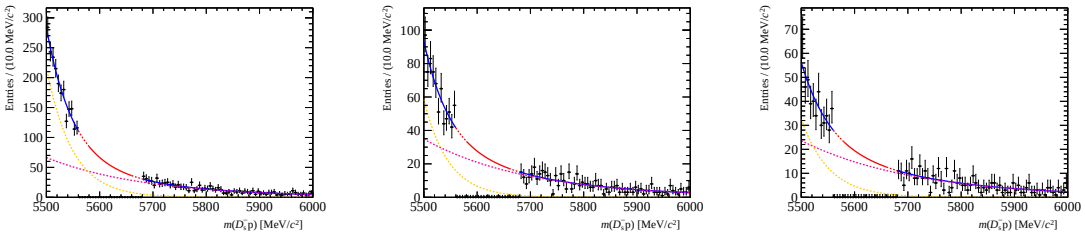

(ah) $(0.7, 0.2)$ **(ai)** $(0.7, 0.4)$ **(aj)** $(0.7, 0.5)$

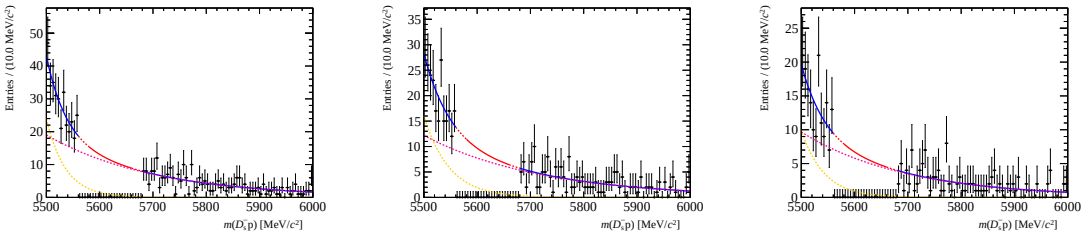

(ak) $(0.7, 0.6)$ **(al)** $(0.7, 0.7)$ **(am)** $(0.7, 0.8)$

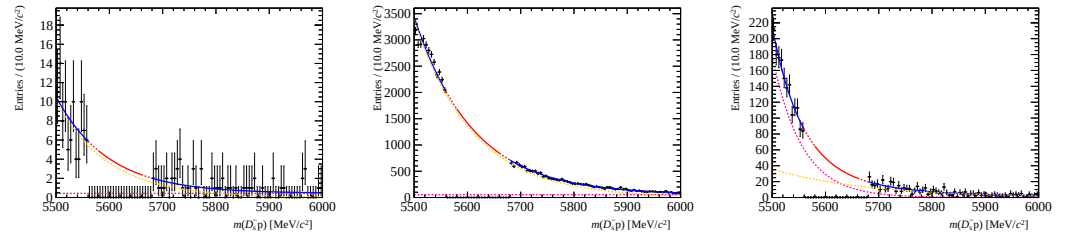

(an) $(0.7, 0.9)$ **(ao)** $(0.9, 0.0)$ **(ap)** $(0.9, 0.2)$

Figure A.2 – Third part of Fig. A.2.

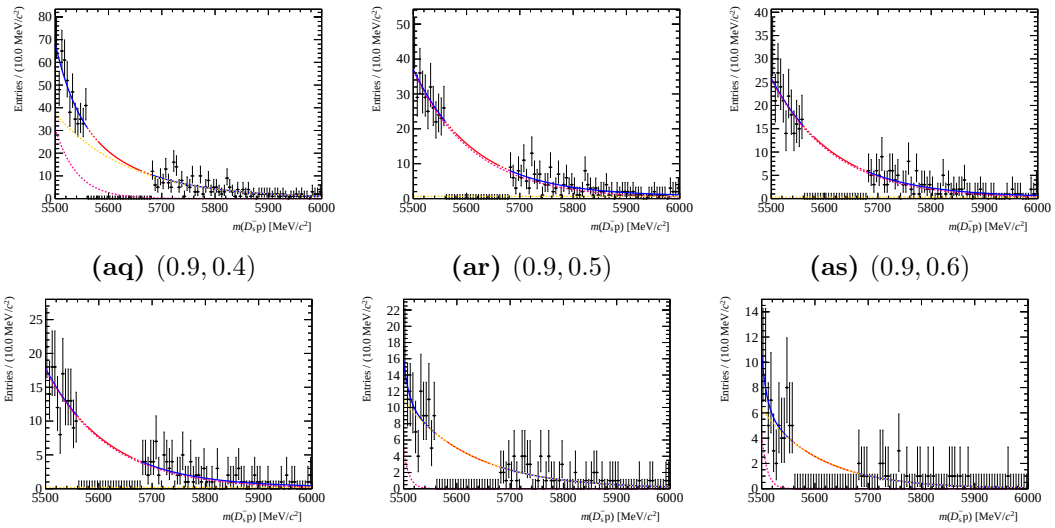

(aq) $(0.9, 0.4)$ **(ar)** $(0.9, 0.5)$ **(as)** $(0.9, 0.6)$

(at) $(0.9, 0.7)$ **(au)** $(0.9, 0.8)$ **(av)** $(0.9, 0.9)$

Figure A.2 – An extended selection of the fits used to estimate the background yield under the signal peak as described in Sec. 3.4.4 for Run 2. The cuts BDT $> \alpha$ and $\text{ProbNN}_p > \beta$ for each figure are displayed as (α, β). In these graphs, the pink and yellow dashed lines are the two exponential functions that describe the background. The blue and red parts are the sum of these two exponential functions. The fit is produced using only the data points that lie in the range of the blue line. The red solid line is used to compute the background events under the signal peak. The red dashed line is ignored in both the fit and the computation of the background events.

Appendix B

Fit templates

B.1 $\Lambda_b^0 \to D_s^- p$ fit

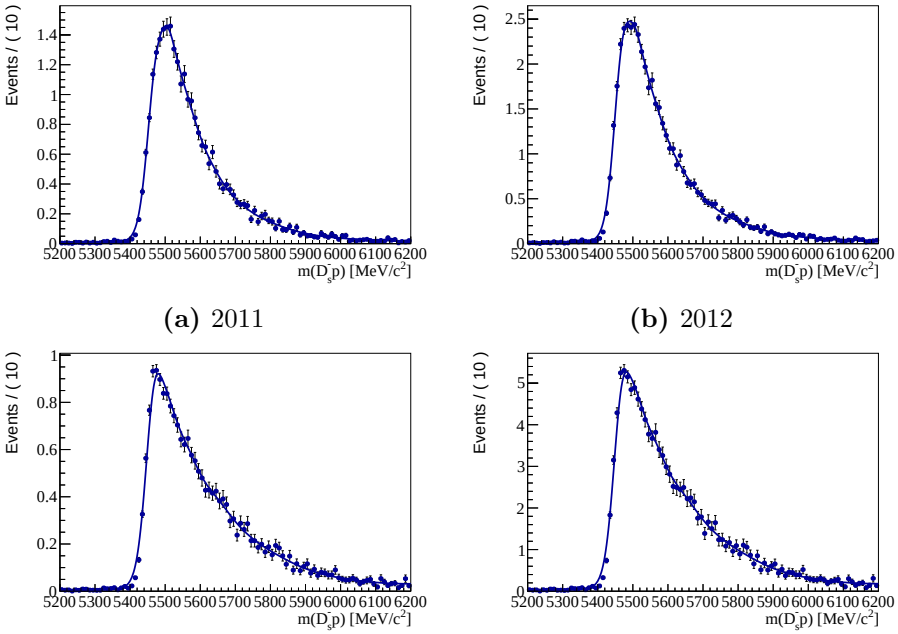

(a) 2011 **(b)** 2012

(c) 2015 **(d)** 2016

Figure B.1 – Background templates for the decay $B_s^0 \to D_s^- K^+$.

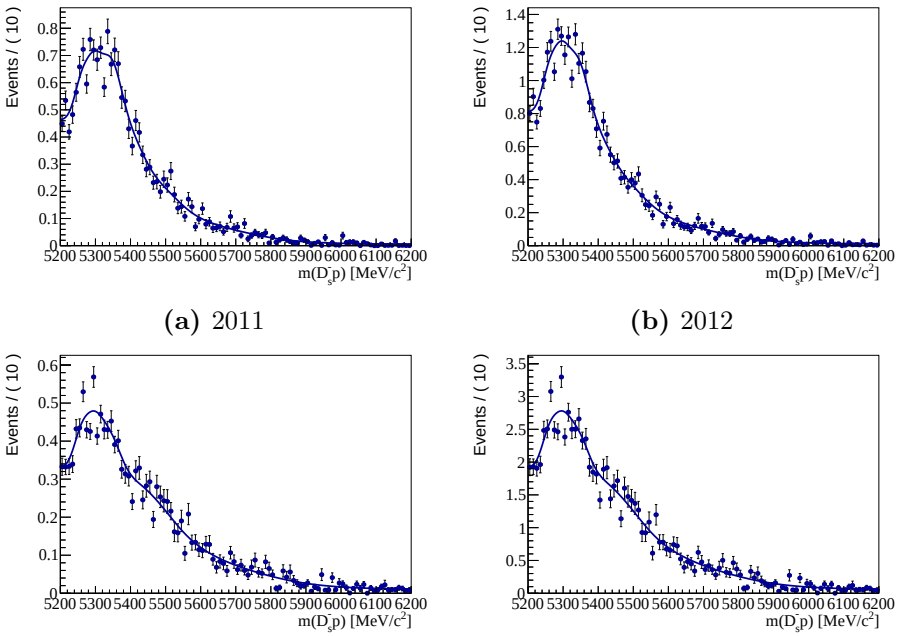

(a) 2011 **(b)** 2012

(c) 2015 **(d)** 2016

Figure B.2 – Background templates for the decay $B_s^0 \to D_s^- K^{*+}$.

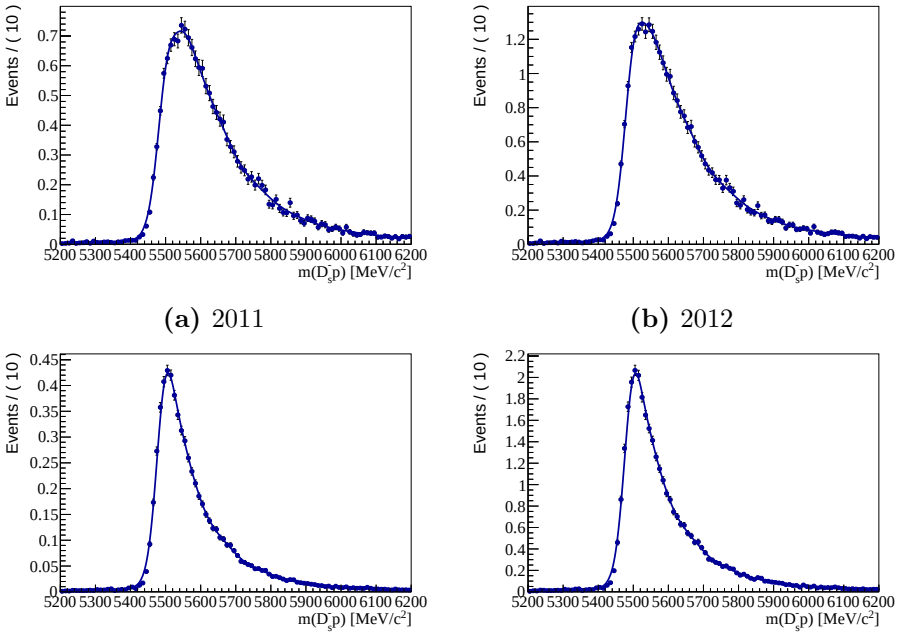

(a) 2011 **(b)** 2012

(c) 2015 **(d)** 2016

Figure B.3 – Background templates for the decay $B_s^0 \to D_s^- \pi^+$.

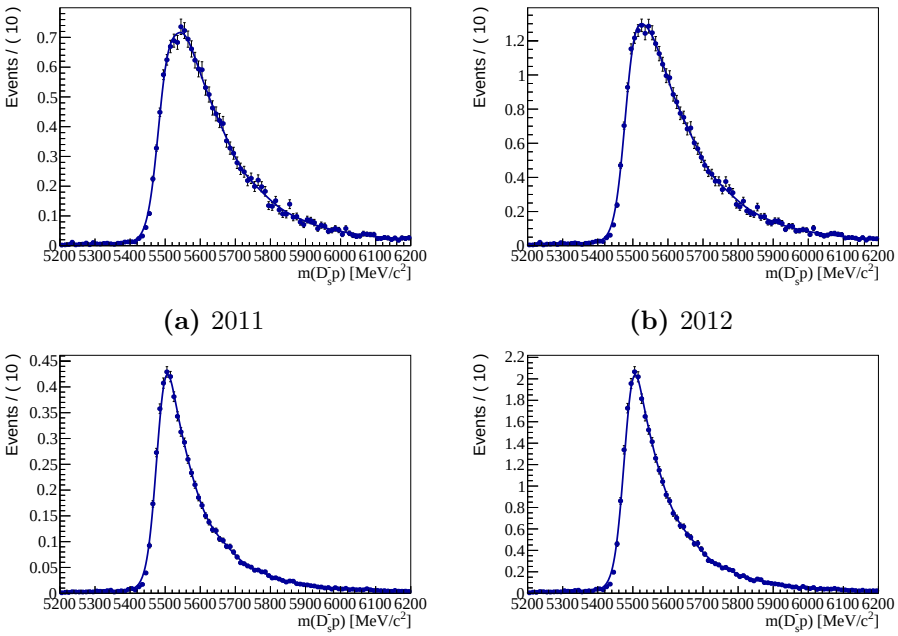

(a) 2011 **(b)** 2012

(c) 2015 **(d)** 2016

Figure B.4 – Background templates for the decay $B_s^0 \to D_s^- \rho$.

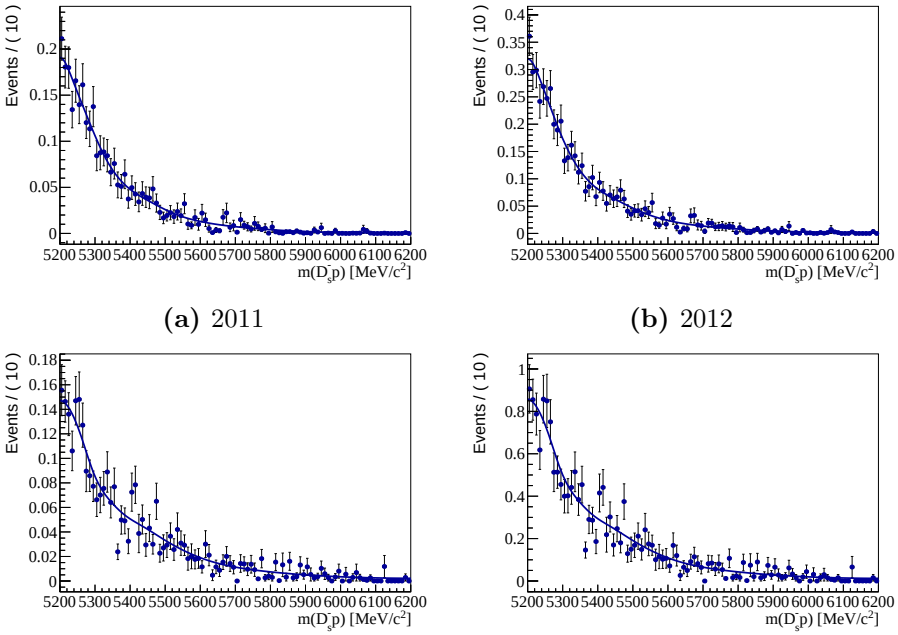

(a) 2011 **(b)** 2012

(c) 2015 **(d)** 2016

Figure B.5 – Background templates for the decay $B_s^0 \to D_s^{*-} K^+$.

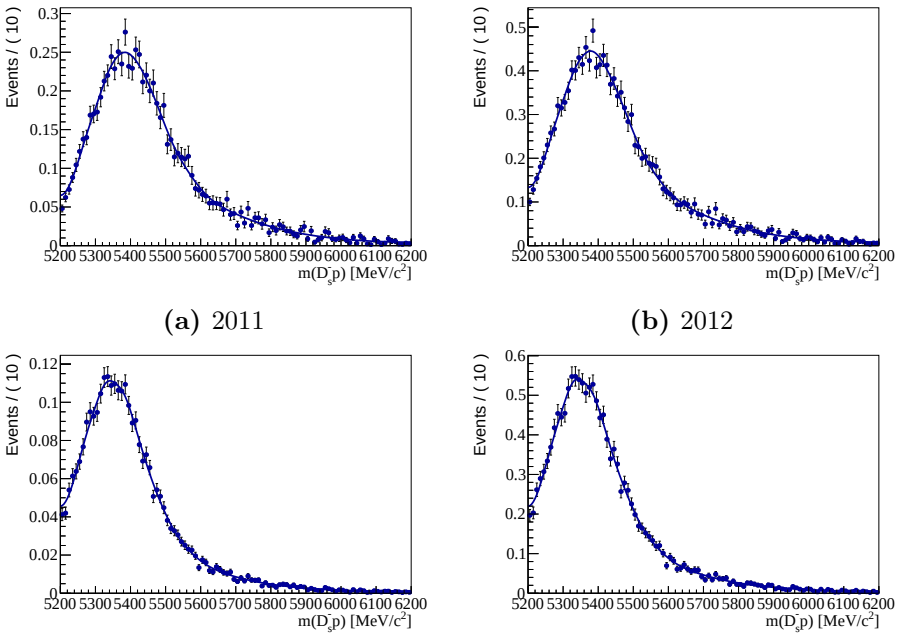

(a) 2011 **(b)** 2012

(c) 2015 **(d)** 2016

Figure B.6 – Background templates for the decay $B_s^0 \to D_s^{*-}\pi^+$.

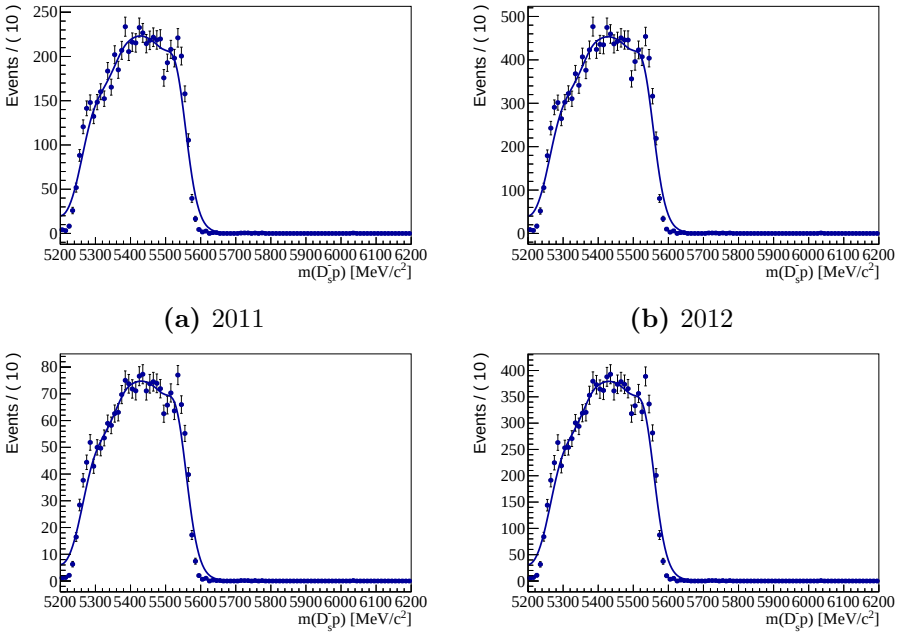

(a) 2011 **(b)** 2012

(c) 2015 **(d)** 2016

Figure B.7 – Background templates for the decay $\Lambda_b^0 \to D_s^{*-}p$.

B.2 $\Lambda_b^0 \to \Lambda_c^+ \pi^-$ fit

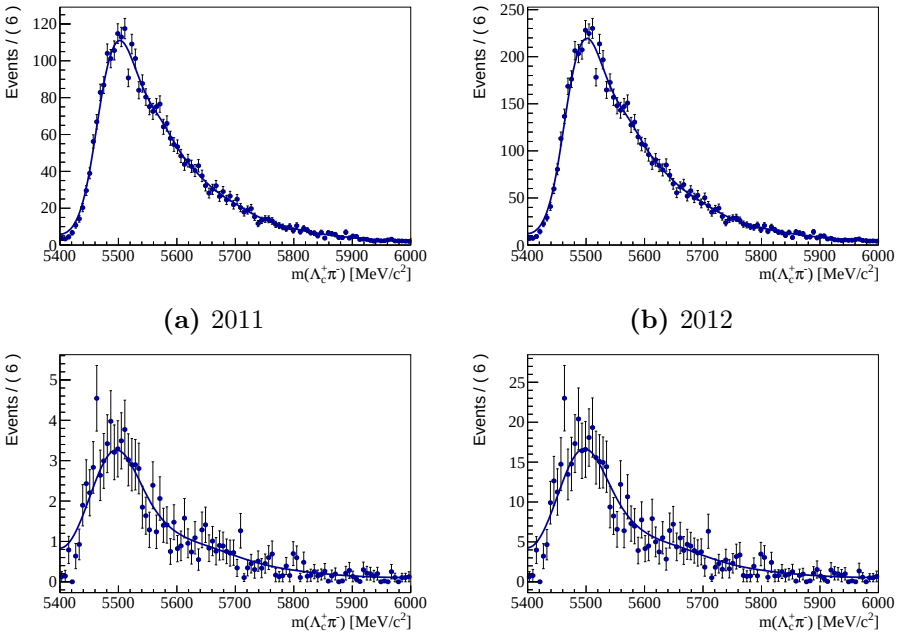

(a) 2011 **(b)** 2012

(c) 2015 **(d)** 2016

Figure B.8 – Background templates for the decay $B^0 \to D^- \pi^+$.

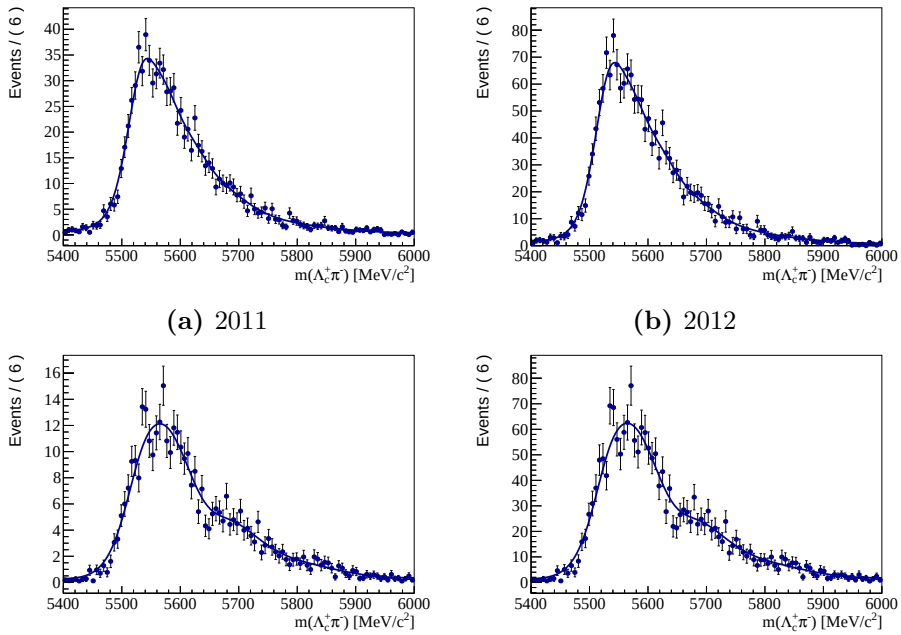

(a) 2011 **(b)** 2012

(c) 2015 **(d)** 2016

Figure B.9 – Background templates for the decay $B_s^0 \to D_s^- \pi^+$.

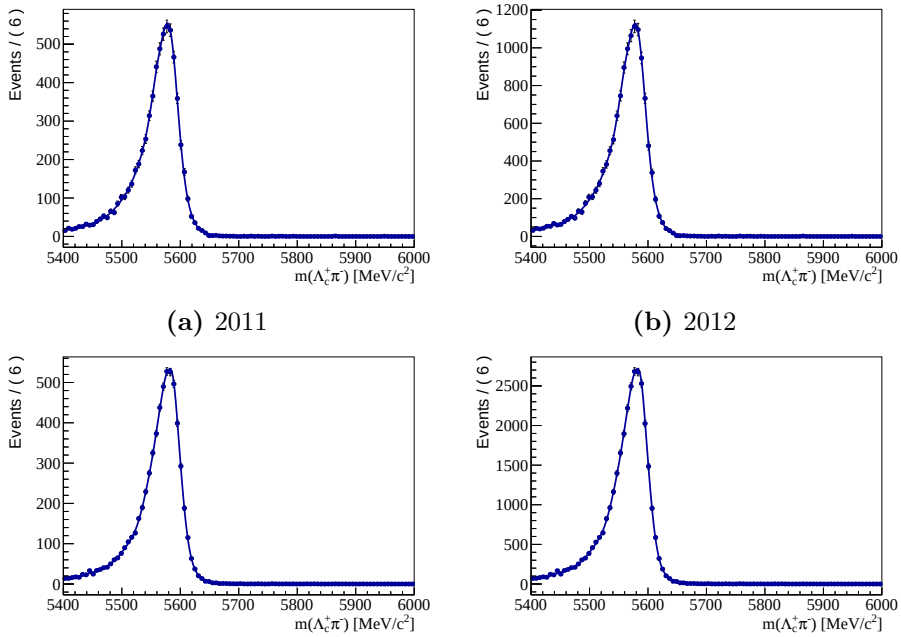

(a) 2011 **(b)** 2012

(c) 2015 **(d)** 2016

Figure B.10 – Background templates for the decay $\Lambda_b^0 \to \Lambda_c^+ K^-$.

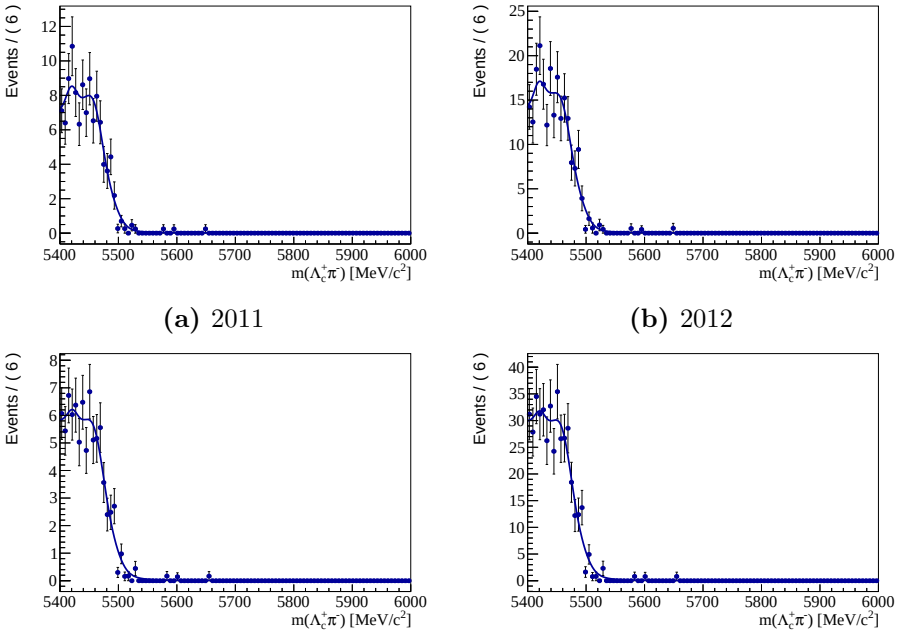

(a) 2011 **(b)** 2012

(c) 2015 **(d)** 2016

Figure B.11 – Background templates for the decay $\Lambda_b^0 \to \Lambda_c^+ \rho$.

Bibliography

[1] *Excellence Universe Cluster*, http://www.universe-cluster.de. Accessed: 2018-05-26.

[2] N. Cabibbo, *Unitary symmetry and leptonic decays*, Phys. Rev. Lett. **10** (1963) 531.

[3] M. Kobayashi and T. Maskawa, *CP-violation in the renormalizable theory of weak interaction*, Progress of Theoretical Physics **49** (1973), no. 2 652.

[4] CKMfitter group, J. Charles *et al.*, *Current status of the Standard Model CKM fit and constraints on $\Delta F = 2$ new physics*, Phys. Rev. **D91** (2015) 073007, arXiv:1501.05013, updated results and plots available at http://ckmfitter.in2p3.fr/.

[5] Particle Data Group, C. Patrignani *et al.*, *Review of particle physics*, Chin. Phys. **C40** (2016) 100001, and 2017 update.

[6] M. Fiore, *New results on semileptonic b decays from LHCb*, arXiv:1511.00105.

[7] T. Mannel and R. Kowalewski, *Semileptonic bottom hadron decays and the determination of V_{cb} and V_{ub}*, P article D ata G roup collaboration, C. Patrignani et al. , Review of Particle Physics, Chin. Phys. C **40** (2016) 100001.

[8] Fermilab Lattice, MILC, J. A. Bailey *et al.*, *$|V_{ub}|$ from $B \to \pi\ell\nu$ decays and (2+1)-flavor lattice QCD*, Phys. Rev. **D92** (2015), no. 1 014024, arXiv:1503.07839.

[9] J. M. Flynn *et al.*, *$B \to \pi\ell\nu$ and $B_s \to K\ell\nu$ form factors and $|V_{ub}|$ from 2+1-flavor lattice QCD with domain-wall light quarks and relativistic heavy quarks*, Phys. Rev. **D91** (2015), no. 7 074510, arXiv:1501.05373.

[10] LHCb, R. Aaij *et al.*, *Searches for Λ_b^0 and Ξ_b^0 decays to $K_S^0 p\pi^-$ and $K_S^0 pK^-$ final states with first observation of the $\Lambda_b^0 \to K_S^0 p\pi^-$ decay*, JHEP **04** (2014) 087, arXiv:1402.0770.

[11] L. Evans and P. Bryant, *LHC machine*, Journal of Instrumentation **3** (2008), no. 08 S08001.

[12] A. Hoecker, *Physics at the LHC run-2 and beyond*, arXiv preprint arXiv:1611.07864 (2016).

[13] T. A. Collaboration, *The ATLAS experiment at the CERN Large Hadron Collider*, Journal of Instrumentation **3** (2008), no. 08 S08003.

[14] T. C. Collaboration, *The CMS experiment at the CERN LHC*, Journal of Instrumentation **3** (2008), no. 08 S08004.

[15] T. A. Collaboration, *The ALICE experiment at the CERN LHC*, Journal of Instrumentation **3** (2008), no. 08 S08002.

[16] LHCb collaboration, A. A. Alves Jr. *et al.*, *The LHCb detector at the LHC*, JINST **3** (2008) S08005.

[17] LHCb, R. Aaij *et al.*, *LHCb Detector Performance*, Int. J. Mod. Phys. **A30** (2015), no. 07 1530022, arXiv:1412.6352.

[18] T. Sjöstrand, S. Mrenna, and P. Skands, *PYTHIA 6.4 physics and manual*, JHEP **05** (2006) 026, arXiv:hep-ph/0603175.

[19] T. Sjöstrand, S. Mrenna, and P. Skands, *A brief introduction to PYTHIA 8.1*, Comput. Phys. Commun. **178** (2008) 852, arXiv:0710.3820.

[20] D. J. Lange, *The EvtGen particle decay simulation package*, Nucl. Instrum. Meth. **A462** (2001) 152.

[21] P. Golonka and Z. Was, *PHOTOS Monte Carlo: A precision tool for QED corrections in Z and W decays*, Eur. Phys. J. **C45** (2006) 97, arXiv:hep-ph/0506026.

[22] Geant4 collaboration, S. Agostinelli *et al.*, *Geant4: A simulation toolkit*, Nucl. Instrum. Meth. **A506** (2003) 250.

[23] Geant4 collaboration, J. Allison *et al.*, *Geant4 developments and applications*, IEEE Trans. Nucl. Sci. **53** (2006) 270.

[24] M. Clemencic *et al.*, *The LHCb simulation application, Gauss: Design, evolution and experience*, J. Phys. Conf. Ser. **331** (2011) 032023.

[25] I. Belyaev *et al.*, *Handling of the generation of primary events in Gauss, the LHCb simulation framework*, J. Phys. Conf. Ser. **331** (2011) 032047.

[26] *The Large Hadron Collider*, https://timeline.web.cern.ch/timelines/The-Large-Hadron-Collider. Accessed: 2018-05-26.

[27] A. Puig, *The LHCb trigger in 2011 and 2012*, LHCb-PUB-2014-046.

[28] A. Satta, *The LHCb L0 trigger and related detectors*, The European Physical Journal C - Particles and Fields **34** (2004) s411.

[29] LHCb collaboration, *LHCb Trigger and Online Technical Design Report*, CERN-LHCC-2014-016. LHCb-TDR-016.

[30] LHCb collaboration, *LHCb trigger system: Technical Design Report*, CERN-LHCC-2003-031. LHCb-TDR-010.

[31] V. V. Gligorov, *A single track HLT1 trigger*, LHCb-PUB-2011-003.

[32] T. Likhomanenko *et al.*, *LHCb topological trigger reoptimization*, J. Phys. Conf. Ser. **664** (2015) 082025.

[33] V. Battista *et al.*, *Measurement of time-dependent CP-violation observables in $B_s^0 \to D_s^{\mp} K^{\pm}$*, LHCb-ANA-2017-037.

[34] Y. Gao *et al.*, *Study of the $\Lambda_b^0 \to \Lambda_c^+ p\bar{p}\pi^-$ decay*, LHCb-ANA-2017-009.

[35] G. Punzi, *Sensitivity of searches for new signals and its optimization*, in *Statistical Problems in Particle Physics, Astrophysics, and Cosmology* (L. Lyons, R. Mount, and R. Reitmeyer, eds.), p. 79, 2003. arXiv:physics/0308063.

[36] L. Anderlini *et al.*, *The PIDCalib package*, Tech. Rep. LHCb-PUB-2016-021. CERN-LHCb-PUB-2016-021, CERN, Geneva, Jul, 2016.

[37] M. Pivk and F. R. Le Diberder, *Plots: A statistical tool to unfold data distributions*, Nuclear Instruments and Methods in Physics Research Section A: Accelerators, Spectrometers, Detectors and Associated Equipment **555** (2005), no. 1-2 356.

[38] R. Brun and F. Rademakers, *ROOT: An object oriented data analysis framework*, Nucl. Instrum. Meth. **A389** (1997) 81.

[39] T. Skwarnicki, *A study of the radiative cascade transitions between the Upsilon-prime and Upsilon resonances*, PhD thesis, Institute of Nuclear Physics, Krakow, 1986, DESY-F31-86-02.

[40] D. M. Santos and F. Dupertuis, *Mass distributions marginalized over per-event errors*, Nuclear Instruments and Methods in Physics Research Section A: Accelerators, Spectrometers, Detectors and Associated Equipment **764** (2014) 150.

[41] N. L. Johnson, *Systems of frequency curves generated by methods of translation*, Biometrika **36** (1949), no. 1/2 149.

[42] A. Martin Sanchez, P. Robbe, and M.-H. Schune, *Performances of the LHCb L0 Calorimeter Trigger*, Tech. Rep. LHCb-PUB-2011-026. CERN-LHCb-PUB-2011-026, CERN, Geneva, Jun, 2012.

[43] R. Fleischer, N. Serra, and N. Tuning, *Tests of Factorization and SU(3) Relations in B Decays into Heavy-Light Final States*, Phys. Rev. **D83** (2011) 014017, arXiv:1012.2784.

[44] J. D. Bjorken, *Topics in B Physics*, Nucl. Phys. Proc. Suppl. **11** (1989) 325.

[45] M. Beneke, G. Buchalla, M. Neubert, and C. T. Sachrajda, *QCD factorization for exclusive, nonleptonic B meson decays: General arguments and the case of heavy light final states*, Nucl. Phys. **B591** (2000) 313, arXiv:hep-ph/0006124.

[46] W. Detmold, C. Lehner, and S. Meinel, $\Lambda_b \to p\ell^-\bar{\nu}_\ell$ *and* $\Lambda_b \to \Lambda_c\ell^-\bar{\nu}_\ell$ *form factors from lattice QCD with relativistic heavy quarks*, Phys. Rev. **D92** (2015), no. 3 034503, arXiv:1503.01421.